

FACULTY
OF MATHEMATICS
AND PHYSICS
Charles University

1

BACHELOR THESIS

2

Martin Vavřík

3

**Simulation and Reconstruction
of Charged Particle Trajectories
in an Atypic Time Projection Chamber**

4

5

Institute of Particle and Nuclear Physics

6

Supervisor of the bachelor thesis: Mgr. Tomáš Sýkora, Ph.D.

7

Study programme: Physics

8

Prague 2025

- ⁹ I declare that I carried out this bachelor thesis independently, and only with the
¹⁰ cited sources, literature and other professional sources. It has not been used to
¹¹ obtain another or the same degree.
- ¹² I understand that my work relates to the rights and obligations under the Act
¹³ No. 121/2000 Sb., the Copyright Act, as amended, in particular the fact that the
¹⁴ Charles University has the right to conclude a license agreement on the use of this
¹⁵ work as a school work pursuant to Section 60 subsection 1 of the Copyright Act.

In date
Author's signature

¹⁶ Dedication.

Title: Simulation and Reconstruction of Charged Particle Trajectories in an Atypical Time Projection Chamber **Added hyphen to avoid overfull hbox**

Author: Martin Vavřík

Institute: Institute of Particle and Nuclear Physics

Supervisor: Mgr. Tomáš Sýkora, Ph.D., Institute of Particle and Nuclear Physics

Abstract: Abstract.

Keywords: key words

¹⁷ Contents

¹⁸	Motivation	2
¹⁹	0.1 ATOMKI Anomaly	2
²⁰	0.1.1 ATOMKI Measurements	2
²¹	0.1.2 Other Experiments	3
²²	0.2 X17 Project at IEAP CTU	5
²³	1 Time Projection Chamber	8
²⁴	1.1 Charge transport in gases	8
²⁵	1.1.1 Drift	8
²⁶	1.1.2 Diffusion	10
²⁷	1.2 Readout	11
²⁸	1.2.1 Multi-Wire Proportional Chamber	11
²⁹	1.2.2 Gas Electron Multiplier	11
³⁰	1.2.3 Micromegas	11
³¹	1.2.4 Parallel Plate Chamber	12
³²	1.3 Orthogonal Fields TPC at IEAP CTU	12
³³	1.3.1 Motivation and Associated Challenges	12
³⁴	1.3.2 Coordinate Systems and Dimensions	13
³⁵	1.3.3 Magnetic Field Simulation	15
³⁶	2 Track Simulation	18
³⁷	2.1 Microscopic Simulation	18
³⁸	2.2 Runge-Kutta Simulation	20
³⁹	3 Track Reconstruction	22
⁴⁰	3.1 Reconstruction Assuming Steady Drift	22
⁴¹	3.2 Ionization Electron Map	24
⁴²	3.2.1 Gradient Descent Algorithm	27
⁴³	3.2.2 Interpolation on the Inverse Grid	28
⁴⁴	3.3 Discrete Reconstruction	30
⁴⁵	4 Energy Reconstruction	32
⁴⁶	4.1 Cubic Spline Fit	32
⁴⁷	4.2 Circle and Lines Fit	34
⁴⁸	4.2.1 Two-dimensional fit	35
⁴⁹	4.2.2 Three-dimensional fit	36
⁵⁰	4.3 Runge-Kutta Fit	38
⁵¹	Conclusion	43
⁵²	Bibliography	46
⁵³	List of Abbreviations	52

⁵⁴ Motivation

⁵⁵ A Time Projection Chamber (TPC) [refs] is a type of gaseous detector that detects
⁵⁶ charged particle trajectories by measuring the positions and drift time of ions cre-
⁵⁷ ated in the gas. The energies of these particles can be inferred from the curvatures
⁵⁸ of their trajectories in the magnetic field (specific field inside the TPC).

⁵⁹ The goal of this thesis is to develop an algorithm for the reconstruction of
⁶⁰ charged particle trajectories and energy in an *atypic* TPC with orthogonal elec-
⁶¹ tric and magnetic fields, hereafter referred to as the Orthogonal Fields TPC
⁶² (OFTPC), used in the X17 project at the Institute of Experimental and Applied
⁶³ Physics, Czech Technical University in Prague (IEAP CTU). Furthermore, we
⁶⁴ present the results of testing of several (gradually improving) developed algo-
⁶⁵ rithms with different samples of simulated data. Put this somewhere, (maybe
⁶⁶ just the abstract?). We use the Garfield++ toolkit [1] for simulations in combina-
⁶⁷ tion with the ROOT framework [2] for data analysis and visualization. Some of
⁶⁸ our more demanding simulations are run on the MetaCentrum grid [3].

⁶⁹ The X17 project in IEAP CTU aims to reproduce measurements of anomalous
⁷⁰ behavior in the angular correlation distribution of pairs produced by the Internal
⁷¹ Pair Creation (IPC) mechanism [4] during the decay of certain excited nuclei
⁷² (⁸Be, ¹²C, and ⁴He) observed by a team at ATOMKI in Hungary. I would leave
⁷³ this here as a short summary before I explain it in more detail in the sections
⁷⁴ below.

⁷⁵ Add citations: X17 project, VdG. Maybe also TPC, etc.

⁷⁶ 0.1 ATOMKI Anomaly

⁷⁷ Many different theories propose the existence of *new light boson(s)* that are weakly
⁷⁸ coupled to ordinary matter [5]. These particles are potential dark matter candi-
⁷⁹ dates and could contribute to a solution of other issues with the Standard Model,
⁸⁰ such as the strong CP problem and the anomalous muon magnetic moment. Mass
⁸¹ range of axions?

⁸² A possible way of detecting such bosons with a short lifetime is to observe
⁸³ nuclear transitions of excited nuclei. If a boson was emitted during the transition
⁸⁴ and subsequently decayed into an electron-positron pair, we could observe this as
⁸⁵ a peak on top of the standard e^+e^- (both cursive and upright forms are used in
⁸⁶ different articles) angular correlation from the Internal Pair Creation (IPC) and
⁸⁷ the External Pair Creation (EPC).

⁸⁸ 0.1.1 ATOMKI Measurements

⁸⁹ Historically, there were several measurements of the IPC in nuclear transitions
⁹⁰ in ⁸Be at Institute für Kernphysik (Frankfurt) [6, 7, 8] and at ATOMKI (De-
⁹¹ brecen, Hungary) [9, 10] resulting in different anomalies with invariant mass in
⁹² the range 5 – 15 MeV. This prompted a development of a better spectrometer at
⁹³ ATOMKI.

⁹⁴ In 2015, a group at ATOMKI observed an anomalous IPC in ⁸Be [11]. They
⁹⁵ used the ⁷Li(p, γ)⁸Be reaction at the $E_p = 1030$ keV proton capture resonance

96 to prepare the 18.15 MeV excited state ($J^\pi = 1^+$, $T = 0$). This state decays
97 predominantly through M1 transitions to the ground state ($J^\pi = 0^+$, $T = 0$) and
98 to the 3.03 MeV state ($J^\pi = 2^+$, $T = 0$) [12]. **Transition figure – all transitions
99 of isotopes? IPC figure?**

100 The angular correlation of the e^+e^- pairs created internally in these transitions
101 were measured and compared to the simulation; results from a narrow $E_{\text{sum}} =$
102 $= 18$ MeV region are shown in Figure 0.1a. The simulation includes boson decay
103 pairs for different boson masses. The disparity parameter y is defined as

$$y = \frac{E_{e^-} - E_{e^+}}{E_{e^-} + E_{e^+}}, \quad (0.1)$$

104 where E_{e^-} and E_{e^+} are the kinetic energies of the electron and positron.

105 Their experimental setup was later upgraded ([details?](#)) and used for new mea-
106 surements. In 2022 the ${}^8\text{Be}$ anomaly was also measured using the $E_p = 441$ keV
107 resonance to produce the 17.64 MeV excited state ($J^\pi = 1^+$, $T = 1$) which again
108 decays primarily to the ground state and the 3.03 MeV state [12]. The anomaly
109 was also measured for $E_p = 650$ and 800 keV where E1 transitions from the direct
110 proton capture dominate [13]. The results for e^+e^- with $E_{\text{sum}} \in [13.5, 20]$ MeV
111 are shown in Figure 0.1b.

112 The newer setup was also used in 2021 to study the ${}^3\text{H}(p, e^+e^-){}^4\text{He}$ reaction at
113 $E_p = 510, 610$ and 900 keV [14], inducing direct and resonant capture populating
114 the overlapping first 20.21 MeV ($J^\pi = 0^+$) and second 21.01 MeV ($J^\pi = 0^-$)
115 excited states [15]. The comparison of simulated and measured e^+e^- pair angular
116 correlations in the $E_{\text{sum}} \in [18, 22]$ MeV region is shown in Figure 0.1c.

117 In 2022, another anomaly was measured in the ${}^{11}\text{B}(p, e^+e^-){}^{12}\text{C}$ process [16].
118 The $E_p = 1388$ keV resonance was used to populate the 17.23 MeV excited state
119 ($J^\pi = 1^-$, $T = 1$) with a large width $\Gamma = 1.15$ MeV [17]. This state decays
120 mainly through E1 transitions to the ground state $J^\pi = 0^+$ and to the 4.44 MeV
121 state $J^\pi = 2^+$. To compensate for energy losses in the target, five energies in
122 the range $E_p = 1.5\text{--}2.5$ MeV were used. The experimental angular correlation for
123 the 17.23 MeV transition to the ground state is shown in Figure 0.1d.

124 Possible explanations of the anomaly include experimental effects, higher or-
125 der processes in the Standard Model [18, 19] or even a protophobic fifth force
126 mediated by a new 17 MeV boson X17 [20]. **Not sure if the introduction should
127 be referenced since even though it is related, it is an independent theory de-
128 veloped only (?) to explain these measurements. Zhang and Miller: <https://www.sciencedirect.com/science/article/pii/S0370269321000010>**

130 0.1.2 Other Experiments

131 Since the ATOMKI measurements, several experiments have been initiated to
132 attempt to replicate the results and search for the hypothetical X17 particle. The
133 following experiments have already produced results. **Could cite the ATOMKI
134 review paper here.**

135 Two-arm e^+e^- spectrometer in Hanoi

136 The anomaly in ${}^8\text{Be}$ has been observed with a high ($> 4\sigma$ **That's all they write
137 in their article.**) confidence by a team at the Hanoi University of Sciences for

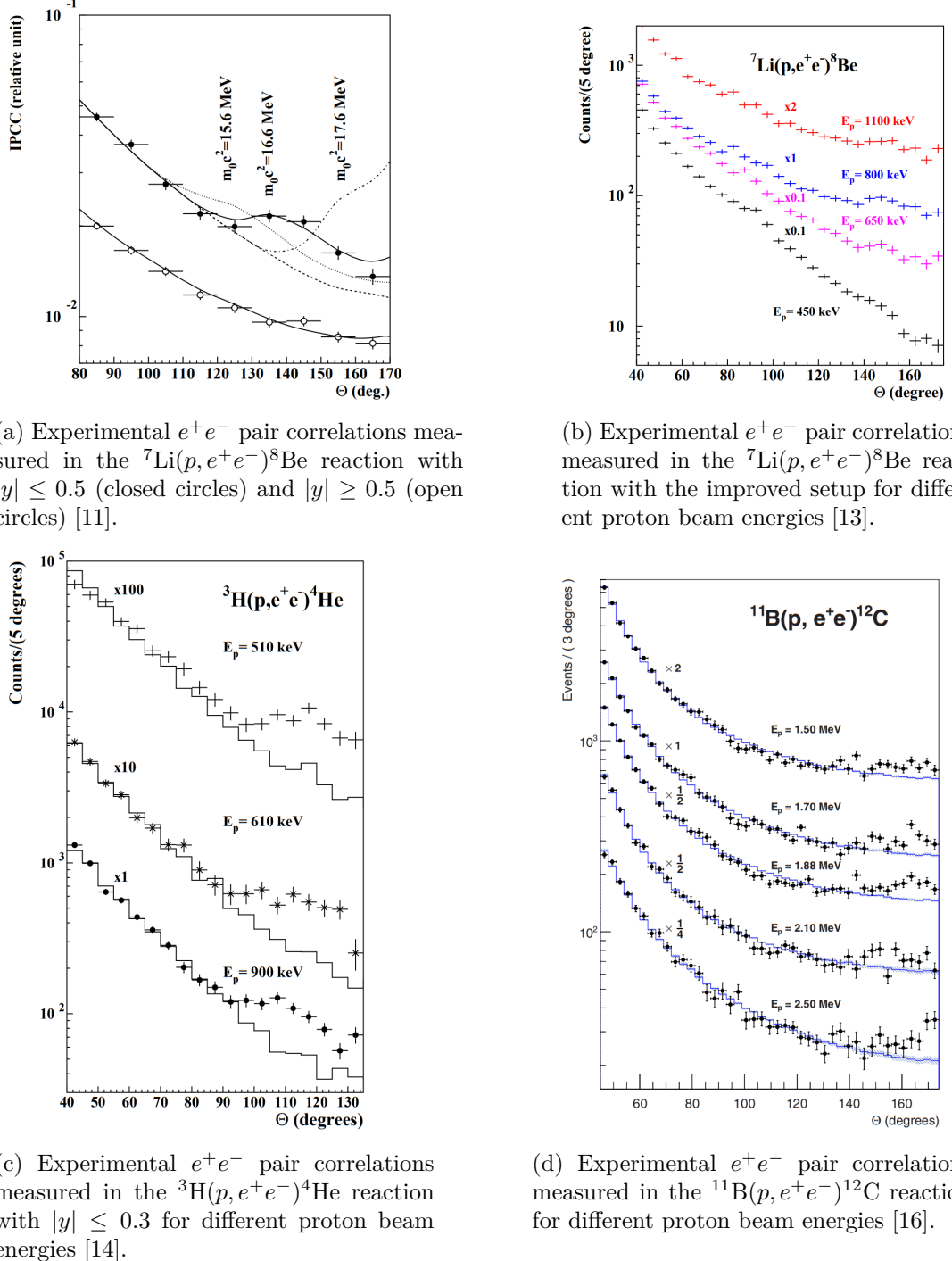


Figure 0.1: The ATOMKI anomalous IPC measured for different nuclei.

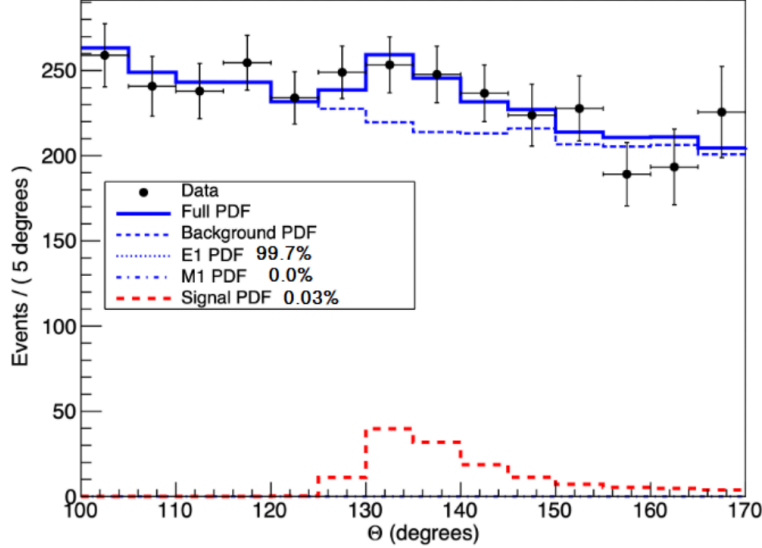


Figure 0.2: Results from the Hanoi spectrometer – angular e^+e^- pair correlations measured in the ${}^7\text{Li}(p, e^+e^-){}^8\text{Be}$ reaction at $E_p = 1225$ keV [21].

138 $E_p = 1225$ keV [21]. They built a two-arm spectrometer in collaboration with
139 ATOMKI and calibrated it using the 17.6 MeV M1 transition. The results are
140 shown in Figure 0.2.

141 Collisions at Nuclotron in Dubna

142 At the Joint Institute for Nuclear Research in Dubna, signal in the form of en-
143 hanced structures in the $\gamma\gamma$ spectra at ~ 17 and 38 MeV invariant masses for
144 $p + \text{C}$, $d + \text{C}$ and $d + \text{Cu}$ reactions at momenta 5.5 , 2.75 , and 3.83 GeV per nu-
145 cleon [22]. Monte Carlo simulations support the conclusion that the signals are
146 a consequence of a decay of unknown particles X17 and E38.

147 The MEG II (Muon Electron Gamma) experiment

148 Experiments using the ${}^7\text{Li}(p, e^+e^-){}^8\text{Be}$ reaction were carried out at the Paul
149 Scherrer Institute with the MEG II superconducting solenoid spectrometer [23].
150 Analysis of the data with $E_p = 1080$ keV exciting both of the resonances (beam
151 fully stopping in the target) found no significant evidence supporting the X17
152 hypothesis, results are shown in Figure 0.3. An upper bound (at 90% confidence)
153 on the X17-to- γ branching ratio was set at $1.2 \cdot 10^{-5}$ for the 18.15 MeV state
154 (larger than the ratio $5.8 \cdot 10^{-6}$ obtained by ATOMKI in 2016). Could add their
155 90% C.L bounds figure also. Insufficient statistics – 6.2 % (1.5σ) p-value.

156 0.2 X17 Project at IEAP CTU

157 The aim of the X17 project at the Van der Graaff facility of the Institute of
158 Experimental and Applied Physics, Czech Technical University in Prague is to
159 repeat the original ATOMKI experiments with ${}^7\text{Li}$ and ${}^3\text{H}$ targets using an inde-
160 pendent e^+e^- spectrometer. In order to effectively measure the anomaly, we need
161 to reconstruct both the energy and the angular correlation of the e^+e^- pairs. The

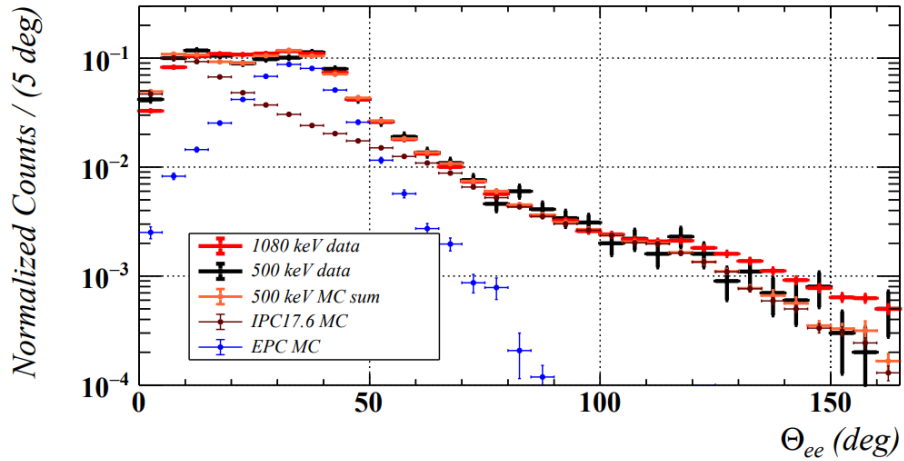


Figure 0.3: Results from the MEG II experiments – angular correlation of e^+e^- pairs with $E_{\text{sum}} \in [16, 20]$ MeV measured in the ${}^7\text{Li}(p, e^+e^-){}^8\text{Be}$ reaction with proton beam energies 500 and 1080 keV. The 500 keV dataset is fitted with Monte Carlo of both the IPC deexcitation and the EPC produced by gammas [23].

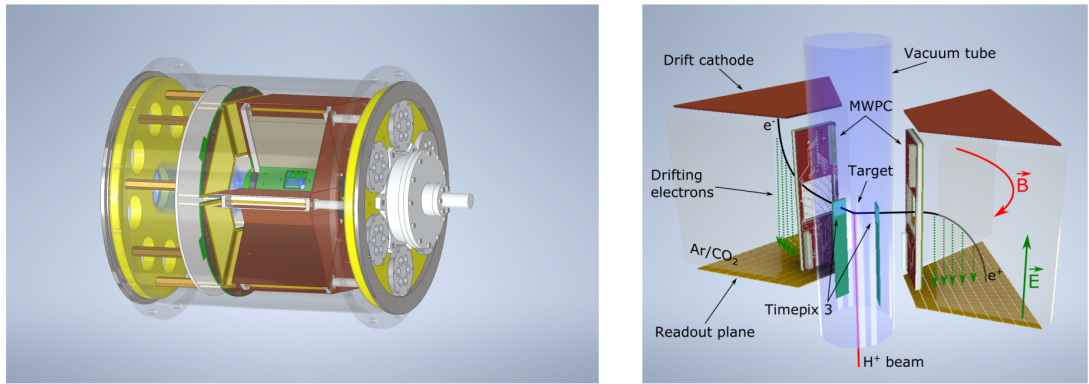


Figure 0.4: Schematics of the detector at the Van der Graaff facility at IEAP CTU.

162 spectrometer will use three layers of detectors to achieve this – Timepix 3 (TPX3)
 163 silicon pixel detector and Multi-Wire Proportional Chamber (MWPC) layers for
 164 the angle reconstruction and a Time Projection Chamber (TPC) layer for the en-
 165 ergy reconstruction. The schematics of the prepared detector is in Figure 0.4
 166 Spectrometer CAD drawing (coordinates here or next chapter?). Cite some VdG
 167 paper, mention grant? Using https://cernbox.cern.ch/pdf-viewer/public/rf0oU1nqVLN3acZ/LuzH_submitted.pdf.

168
 169 The energy of e^+e^- pair produced in the reaction is given by the energy
 170 available E_r in the reaction and can be distributed between them arbitrarily.
 171 Nonetheless in the decay of the hypothetical X17 particle, electron and positron
 172 should have similar energy and we can therefore use a disparity cut $|y| \leq 0.5$
 173 for the disparity parameter (defined in Equation 0.1). Interesting events should
 174 rarely have a particle with an energy below $E_r/4$ (roughly 4 MeV). Electrons with
 175 such low energies are scattered significantly by even a thin layer of relatively light
 176 material, for this reason the TPX3 layer will be inside of the vacuum tube and

177 the tube will have a thinned aluminum segment or KaptonTM windows.

178 TPX3 can measure (in each $55 \times 55 \mu\text{m}$ pixel of its 256×256 grid) time-of-arrival
179 (ToA) with 1.6 ns precision and time-over-threshold (ToT) which reflects the de-
180 posited energy. This potentially allows 3D tracking if we increase the chip thick-
181 ness at the cost of increased scattering. The layer can reconstruct the reaction
182 vertex and the angular correlation with high precision.

183 The layer of MWPCs with sensitive area $40 \times 38 \text{ mm}^2$ will be outside of
184 the beam pipe. It will provide an extra point on the particle trajectory which can
185 help with the estimation of the reaction vertex and improve the TPC performance
186 by providing its entry point.

187 The TPCs, which are a subject of this theses, are in a magnetic field of per-
188 manent magnets positioned between them and provide 3D track reconstruction
189 and subsequent momentum and particle identification (its charge, or even type
190 based on its stopping power). They avoid radiative losses thanks to the small
191 interaction with the incident particle. For the readout, triple Gas Electron Mul-
192 tiplier (GEM) will be used. The magnetic field layout in our TPCs is atypical –
193 orthogonal to the electric field inside the chamber, this is why we call them Or-
194 thogonal Fields TPC (OFTPC). Further details about our OFTPCs are provided
195 in section 1.3.

1. Time Projection Chamber

Using (2010 – a little old) <https://cds.cern.ch/record/1302071/files/CERN-PH-EP-2010-047.pdf>

A Time Projection Chamber (TPC) is a type of gaseous detector that uses the drift in an electric field of free charges (electrons and cations, also anions if attachment of electrons to the gas particles is considered) produced by an ionizing particle to reconstruct its 3D trajectory. When placed inside a magnetic field, the momentum of the incident particle can be inferred from the curvature of its trajectory. Particle identification is also possible using the ionization energy loss inside the TPC (see Figure 1.1). The detector used 80:20 Ar:CH₄ mixture at 8.5 atm pressure.

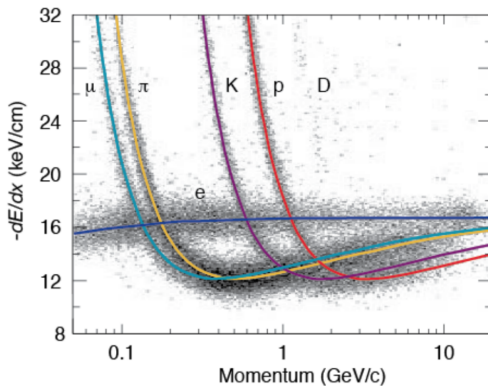


Figure 1.1: Particle identification in the PEP-4 TPC at SLAC based on the energy loss per distance $\frac{dE}{dx}$ [24].

The original TPC used in the PEP-4 experiment at SLAC (Figure 1.2) was a 2×2 m cylinder with a central cathode that produced a strong electric field, making the ionization electrons drift towards one of the bases. The readout consisted of MWPCs, where electrons are accelerated towards the anode wires enough to further ionize the gas and cause an avalanche.

When a charged particle crosses the volume of a TPC, it loses energy by excitation and ionization of the detector gas (how much – from dE/dx + density → footnote?). Most ionizing collision produce a single ionization electron, sometimes a few secondary electrons are produced close to the collision vertex. In rare cases, the ionization electron has energy large enough to create a measurable track, such an electron is called a δ -electron (terminology, just like below – technically it's a (primary) ionization electron causing other (secondary) ionization). Penning transfer (collisions, light – factor 10 for gas gain in Ar/CO₂ viz PDG CERN)?

CERES/NA45 – very inhomogeneous magnetic field

1.1 Charge transport in gases

1.1.1 Drift

Produced ionization electrons (terminology – called ionization electrons in the rest of the thesis, ionoelectrons?) are accelerated towards the readout by the electric

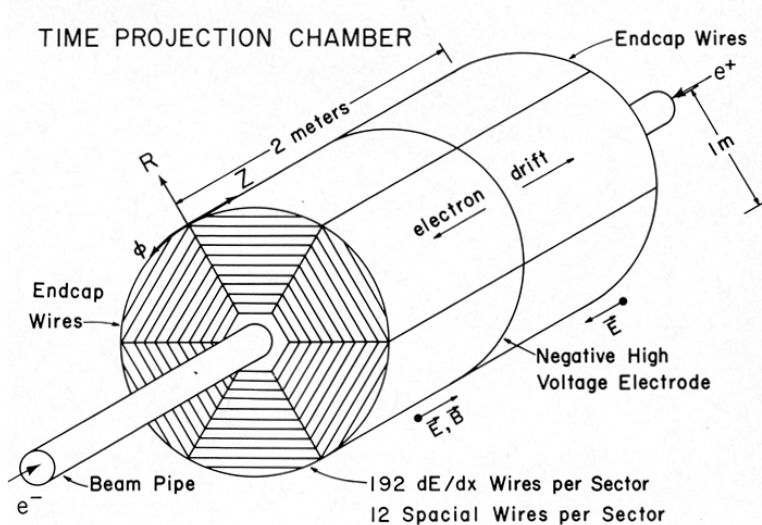


Figure 1.2: Schematic view of the PEP-4 TPC [25]. A charged particle produced in a collision in the beam pipe creates a spiral ionization track in the magnetic field. The central cathode then accelerates ionization electrons towards the endcap anode wires where they are multiplied and read out.

225 field inside the chamber. At the same time, they lose speed by colliding with
 226 the gas particles, quickly reaching a constant (for a given field \mathbf{E}, \mathbf{B}) mean drift
 227 velocity. The electrons might be absorbed by electronegative impurities, such as
 228 halides and oxygen.

229 In many gases (called "hot", e.g., Ar or CH_4), the drift velocity (def? the
 230 paragraph above not enough?) is much greater than that of their thermal motion
 231 thanks to a high proportion of elastic collisions. On the other hand, "cold"
 232 gases like CO_2 have a higher proportion of inelastic collisions (e.g., thanks to
 233 the excitation of rotational and vibrational states) and therefore much lower
 234 (value? magnitude (implied)?) drift velocity.

235 The ions produced by the ionization lose a significant portion of their energy
 236 during each collision since their mass is close to the mass of the gas particles (see
 237 the source material – average energy loss during collision $\Delta E = \frac{2m_i M}{(m_i + M)^2}$, this way
 238 it's more accurate). This, together with their large collision cross section, makes
 239 their drift velocity much smaller and their energy is close to thermal. Since their
 240 momenta aren't randomized to such an extent during collisions, their diffusion
 241 is smaller (more in the sense of distribution of positions, could move this to the
 242 diffusion subsection).

243 The drift is also influenced by the magnetic field. Langevin derived a good
 244 approximation for the drift velocity vector:

$$\mathbf{v}_d = \left(\frac{\mathbf{E}}{\|\mathbf{E}\|} + \omega\tau \frac{\mathbf{E} \times \mathbf{B}}{\|\mathbf{E}\| \|\mathbf{B}\|} + \omega^2\tau^2 \frac{\mathbf{E} \cdot \mathbf{B}}{\|\mathbf{E}\| \|\mathbf{B}\|} \cdot \frac{\mathbf{B}}{\|\mathbf{B}\|} \right) \frac{q\tau}{m(1 + \omega^2\tau^2)} \|\mathbf{E}\|, \quad (1.1)$$

245 where q is the charge of the particle, m is its mass, τ is the mean time between col-
 246 lisions and $\omega = \frac{q}{m} \|\mathbf{B}\|$ is the Larmor frequency. In a standard TPC, \mathbf{E} is nearly
 247 parallel to \mathbf{B} and the influence of the magnetic field on the drift is minimal.
 248 The drift of ions is only negligibly influenced by the magnetic field ($\omega\tau \sim 10^{-4}$ is

²⁴⁹ small due to the low drift velocity – better because it takes τ into account and
²⁵⁰ differs only by E/B ratio). Lorentz angle for orthogonal fields $\tan \psi = -\omega\tau$ (de-
²⁵¹ viation from electric field) – mention in the OFTPC section. Without magnetic
²⁵² field, we can write

$$\mathbf{v}_d = \frac{q\tau}{m} \mathbf{E} = \mu \mathbf{E}, \quad (1.2)$$

²⁵³ where μ is called charge mobility.

²⁵⁴ 1.1.2 Diffusion

²⁵⁵ Due to collisions a cloud of electrons or ions originating from the same point will
²⁵⁶ show a Gaussian density distribution at time t while drifting in the electric field
²⁵⁷ $\mathbf{E} = (0, 0, E_z)$ along the z -coordinate (coordinates defined by the electric field):

$$\rho(x, y, z, t) = (4\pi Dt)^{-\frac{3}{2}} \exp\left(-\frac{x^2 + y^2 + (z - v_d t)^2}{4Dt}\right), \quad (1.3)$$

²⁵⁸ where the diffusion coefficient D can be expressed as

$$D = \frac{\lambda^2}{3\tau} = \frac{\lambda v_d}{3} = \frac{v_d^2 \tau}{3} = \frac{2\varepsilon\tau}{3m}, \quad (1.4)$$

²⁵⁹ where λ is the mean free path and ε the mean energy. The lateral diffusion width
²⁶⁰ σ_x after a drift distance L can be expressed as

$$\sigma_x^2 = 2Dt = \frac{4\varepsilon L}{3qE}. \quad (1.5)$$

²⁶¹ The minimal diffusion width is given by the lowest possible energy of the particles
²⁶² $\varepsilon_{\text{th}} = \frac{3}{2}kT$ (corresponding to thermal motion):

$$\sigma_{x, \text{min}}^2 = \frac{2kTL}{qE}. \quad (1.6)$$

²⁶³ For electrons in "cold gases" (e.g., Ar/CO₂ mixture), the diffusion approaches
²⁶⁴ this limit up to a certain field intensity (~ 100 V/cm at 1 atm pressure)¹. In
²⁶⁵ reality, the transversal diffusion of electrons can differ significantly from their
²⁶⁶ longitudinal diffusion and simulations are necessary to get a precise result.

²⁶⁷ In most TPCs, the transversal (but not the longitudinal) diffusion is reduced
²⁶⁸ by the magnetic field, since it is parallel to the electric field and curves the dif-
²⁶⁹ fusing electrons around their mean trajectory:

$$\frac{D_T(B)}{D_T(0)} = \frac{1}{C + \omega^2 \tau_2^2}, \quad (1.7)$$

²⁷⁰ where C and τ_2 are parameters dependent on the gas used. At low intensity of
²⁷¹ the magnetic field, we can use an approximation $C \approx 1$ and $\tau_2 \approx \tau$.

¹For us $\sigma_{x, \text{min}} = 0.45$ mm, quite close to the actual diffusion 0.5-0.7 mm – details of the calculation.

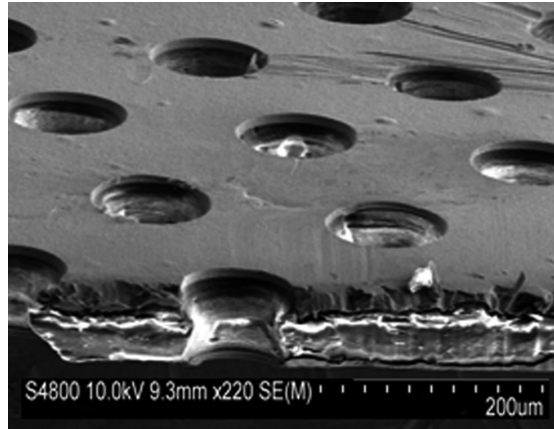


Figure 1.3: A scanning electron microscope image of a GEM foil. [Ref]

272 1.2 Readout

273 1.2.1 Multi-Wire Proportional Chamber

274 In most (2010 – almost all) TPCs operated in experiments Multi-Wire Proportional Chamber (MWPC) (actually wire chamber – similar) was used for the readout. The electrons enter the chamber through a cathode grid and get accelerated in the strong electric field towards the thin anode wires and create a Townsend avalanche (ref), multiplying the signal. Alternating with field wires? That is the difference between MWPC and a drift chamber? The trajectory can be reconstructed using signal from each separate wire. Segmented cathode is also often used for the readout of produced cations. Gating grid (reduction of space charge effect, blocking backflow of ions?, closed for electrons $B=0$, ΔV , static mode (loss of 25% el.) x opening on trigger)? (gas amplification > 10000 required for good SNR, 100-200 ns shaping time), figure – field (acts as a plane from far away and the field only gets strong enough for avalanches)?

286 1.2.2 Gas Electron Multiplier

287 A Gas Electron Multiplier (GEM) is a thin metal-coated polymer sheet with a high density of small holes (Figure 1.3). The amplification is achieved by applying voltage on the metal layers, creating a strong electric field inside the holes and causing avalanches (see Figure 1.4). Double or triple stack of GEMs is usually used to create a sufficient gain. From the last foil, the electrons drift to a segmented anode where the signal is read. The backflow of cations is reduced compared to MWPC. Typical parameters (vs thick GEM?).

294 1.2.3 Micromegas

295 In a MICRO-MEsh GAseous Structure (Micromegas) (in sources I viewed it is not capitalized) electrons pass through a fine mesh (made out of very thin wires) into the narrow amplification gap where they are multiplied in the high field and read as signal on the segmented anode. Very high field ($30-80 \text{ kV/cm}^2$) is necessary to achieve sufficient gain. Cation backflow is heavily suppressed by the mesh.

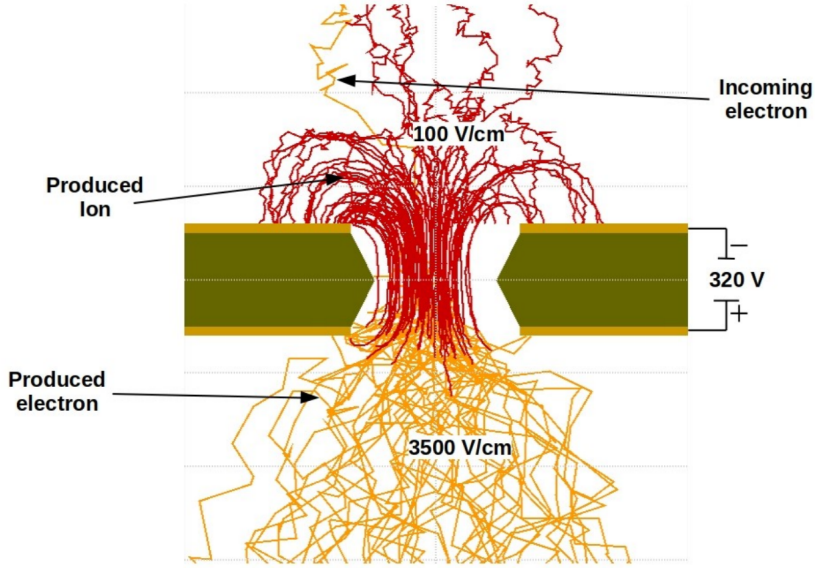


Figure 1.4: Garfield simulation of an avalanche in a GEM hole [26]. An incoming electron (orange) is accelerated in the strong electric field of the GEM and causes further ionization multiplying the number of free electrons (orange). Most of the produced cations (red) are captured by the GEM cathode.

300 1.2.4 Parallel Plate Chamber

301 ... micowell? – these readouts and Micromegas are not used in our detector,
 302 so maybe just mention them at the beginning of the readout section without
 303 excessive detail (some subfigures showing how they look without describing each
 304 too much)

305 1.3 Orthogonal Fields TPC at IEAP CTU

306 At IEAP CTU, we are going to use six identical atypical TPCs with inhomogeneous
 307 toroidal magnetic field **orthogonal** to the electric field ([details below](#)),
 308 hereafter referred to as Orthogonal Fields TPC (OFTPC). It has the shape of
 309 isosceles trapezoidal prism 16 centimeters high with triple-GEM readout on one
 310 of its bases. Dimensions of the OFTPC are discussed in detail in section 1.3.2
 311 below. Throughout this thesis, we assume a uniform electric field along the z axis
 312 with $E_z = -400 \text{ V/cm}$. [Gas mixture used in the detector \(70/30\)](#) and its effect
 313 – some graph with the mixture.

314 1.3.1 Motivation and Associated Challenges

315 The reasons for the unusual field layout are mostly cost related:
 316 a) we use permanent magnets instead of a solenoid and parallel fields are
 317 difficult to accomplish this way,
 318 b) granularity of the TPC readout is limited in order to fit one SAMPA/SRS
 319 hybrid in each sector – parallel fields would bend the trajectories parallel
 320 to the readout requiring more pads and different architecture.

321 In this thesis, we will show that such a setup can reach a similar energy resolution
322 as common cylindrical TPCs while reducing the overall cost.

323 The layout introduces two complications to the track reconstruction – the
324 trajectory in inhomogeneous field is not circular and the drift is distorted by the
325 magnetic field as shown in the Equation 1.1(in our case $\omega\tau \approx 0.08$ for 0.3 T
326 assuming $\mu \approx 0.25 \text{ T}^{-1}$, varies inside the detector). We will deal with these
327 effects in the upcoming chapters.

328 The diffusion in such setup is larger since parallel orientation reduces diffusion
329 by curling the electrons in the x - y direction (see Equation 1.7), but for our
330 relatively weak magnetic field and short drift distance, the difference is negligible.

331 1.3.2 Coordinate Systems and Dimensions

332 In order to describe events in our detector, we use three distinct spaces: the de-
333 tector space \mathcal{D} , the readout space \mathcal{R} and the pad space \mathcal{P} (different spaces that
334 describe different things and each has their own coordinate system, so maybe
335 rename the section somehow?). Each space is later used to represent ionization
336 electrons at different stages of the detection process: their creation in the gas,
337 their final position when hitting the readout plane, and finally their representation
338 in the discrete pad space.

339 Detector Space

340 The detector space \mathcal{D} represents the physical space of our detector. We de-
341 scribe it using Cartesian coordinates (x, y, z) . The z -axis is the detector's axis of
342 symmetry, with its negative direction aligned with the proton beam. The origin
343 $(0, 0, 0)$ is located at the center of the irradiated target. The positive x -axis passes
344 through the center of one the OFTPCs along the intersection of its two planes
345 of symmetry. The y -axis is then chosen to maintain a right-handed coordinate
346 system.

347 Since the detector has a hexagonal symmetry, we use only one of its sectors
348 in this work – the first sector $\mathcal{D}_1 \subset \mathcal{D}$ which is defined by the condition:

$$(x, y, z) \in \mathcal{D}_1 \Leftrightarrow |y| \leq x \tan \frac{\pi}{6}. \quad (1.8)$$

349 Simulations in this sector can be applied to all sectors by rotating the coordinates
350 accordingly. The volume of the OFTPC in this sector, which has the shape of
351 a trapezoidal prism, has these boundaries:

$$x \in [x_{\min}, x_{\max}] = [6.51, 14.61] \text{ cm}, \quad (1.9)$$

$$z \in [z_{\min}, z_{\max}] = [-8, 8] \text{ cm}, \quad (1.10)$$

$$y_{\max}(x_{\min}) = -y_{\min}(x_{\min}) = 2.75 \text{ cm}, \quad (1.11)$$

$$y_{\max}(x_{\max}) = -y_{\min}(x_{\max}) = 7.45 \text{ cm}, \quad (1.12)$$

352 where $y_{\max}(x)$ is the maximal value of the y -coordinate for a given x . The read-
353 out is located at $z = 8$ cm; for some purposes, we also define the distance to
354 the readout $d_r = 8 \text{ cm} - z$ as an alternative to the z -coordinate. Keeping this
355 paragraph as it is because the OFTPC volume is distinct from the first sector
356 and some parts of this thesis use the space beyond this volume.

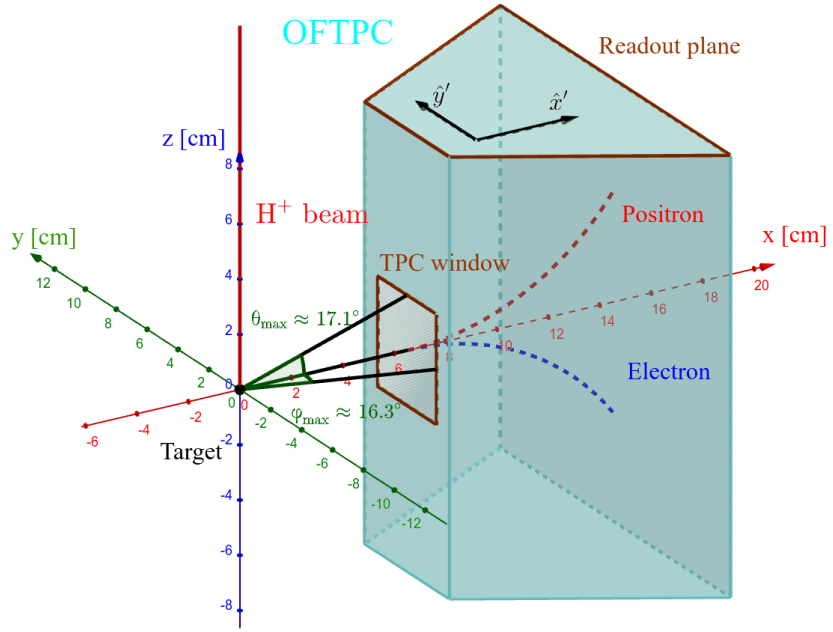


Figure 1.5: Schematics of the first sector OFTPC with detector space coordinates.

357 We also use spherical coordinates (r, θ, φ) with θ measured relative to the xy
 358 plane.

359 Readout Space

360 The readout space \mathcal{R} represents the drift time and final positions of ionization
 361 electrons as measured by an ideal continuous readout. We describe it using
 362 coordinates (x', y', t) , where x' and y' correspond to the detector coordinates at
 363 the readout plane ($z = 8$ cm).

364 Currently not entirely sure how to put this into a figure since only x' and
 365 y' correspond to the detector coordinates, **it will make more sense when**
 366 **visualizing the map**. The drift time t is approximately proportional to d_r .

367 Pad Space

368 The pad space \mathcal{P} represents the time bin and pad number of ionization electrons
 369 as measured by an ideal discrete readout:

$$\mathcal{P} = \{(n_{\text{pad}}, n_t) \in \mathbb{N}^2 \mid n_{\text{pad}} \leq 128\}. \quad (1.13)$$

370 **Rewrite to reflect this:** Technically both values can be zero as defined in
 371 the code (max channel 127). It is not really a subspace of \mathcal{R} but there is a
 372 mapping from \mathcal{R} to \mathcal{P} . It is a discretization of a part of \mathcal{R} , the mapping can be
 373 adjusted depending on the simulation. If we assume uniform electric field there
 374 will be gaps, we don't use gaps in the reconstruction since the electrons should
 375 be pulled towards the pads.

376 The readout of the OFTPC will consist (is the design final?) of 128 rectangular
 377 pads arranged in a staggered pattern. Parameters of the pad layout are shown
 378 in Figure 1.6. The bottom left corner of n -th pad has coordinates $(x_{1,n}, y_{1,n})$,

379 the top right ($x_{2,n}, y_{2,n}$) and its center has coordinates ($x_{c,n}, y_{c,n}$). The gap
 380 between neighboring pads is $g = 0.08$ cm. Time will be read out in discrete bins
 381 of size $t_{\text{bin}} = 100$ ns (details?). Could also describe pad-related functions.

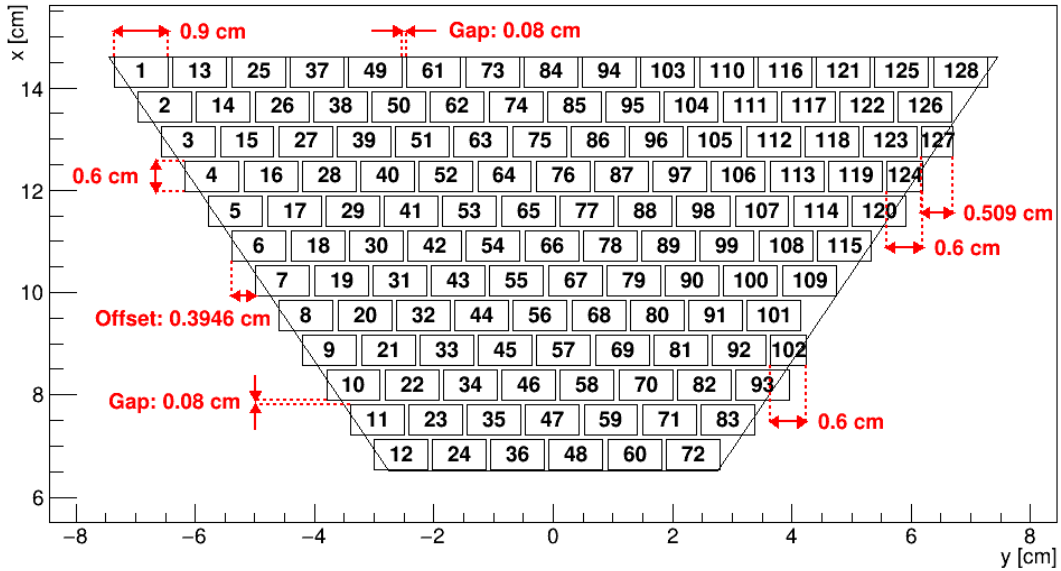


Figure 1.6: Pad layout of the OFTPC and its parameters. Pads 102, 124 and 127 are irregular, the rest has the same dimensions.

382 1.3.3 Magnetic Field Simulation

383 The magnetic field inside our detector is produced by six permanent magnets. It
 384 was simulated using Ansys Maxwell (citation) which gives us values on a regular
 385 grid. More details, vacuum tube, magnets (homogeneous?, density?). Visualization
 386 of the magnetic field is shown in Figure 1.7. Whenever we need to work with
 387 values outside this grid, we use trilinear interpolation described below.

388 Trilinear Interpolation

389 Trilinear interpolation is a 3D generalization of linear interpolation². It can be
 390 used to interpolate a function whose values are known on a regular grid with
 391 rectangular prism cells. We use this simple method for interpolating the magnetic
 392 field, and it is later used in Section 3.2.1 to interpolate the Ionization Electron
 393 Map, a key component of our track reconstruction algorithm. In both cases, we
 394 use a regular cubic grid (apparently it is also called a Cartesian grid).

395 Let us consider a cell of our regular grid (a cube) with an edge of length a
 396 containing the point $\mathbf{C} = (x, y, z)$ where we want to interpolate a function
 397 $f: \mathbb{R}^3 \rightarrow \mathbb{R}$. We know the values of this function at the vertices of the cell
 398 $\mathbf{C}_{ijk} = (x_0 + ia, y_0 + ja, z_0 + ka)$, where $\mathbf{C}_{000} = (x_0, y_0, z_0)$ is the origin of the cell
 399 (is that clear?), and $i, j, k \in \{0, 1\}$ are indices. We also define the points $\mathbf{C}_{ij} =$
 400 $= (x, y_0 + ia, z_0 + ja)$ and $\mathbf{C}_i = (x, y, z_0 + ia)$. Then the interpolated value $\hat{f}(\mathbf{C})$

²Linear interpolation in point $x \in (x_1, x_2)$ of a function $f: \mathbb{R} \rightarrow \mathbb{R}$ known in points $x_1 < x_2$ is the convex combination $\hat{f}(x) = (1 - x_d)f(x_1) + x_d f(x_2)$, where $x_d = \frac{x - x_1}{x_2 - x_1} \in (0, 1)$.

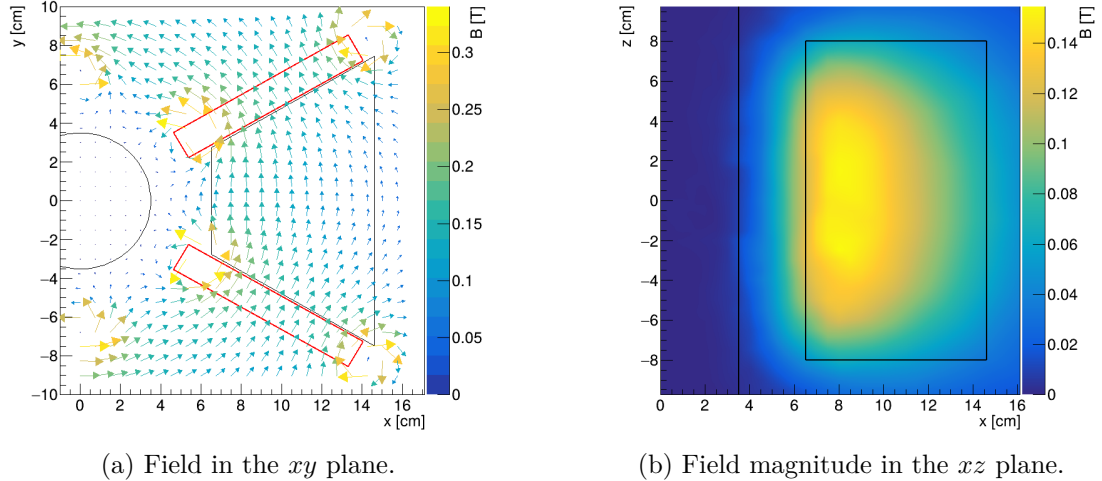


Figure 1.7: Magnetic field simulation results. The OFTPC volume and the vacuum tube are marked with black lines, the magnets are marked with red lines. The coordinates of the magnets from the CAD drawing seem to be 9/10 of the ones from the magnetic simulation (confirm and fix).

401 can be calculated as a composition of three linear interpolations (see Figure 1.8):

$$\hat{f}(\mathbf{C}_{ij}) = (1 - x_d) f(\mathbf{C}_{0ij}) + x_d f(\mathbf{C}_{1ij}), \quad (1.14)$$

$$\hat{f}(\mathbf{C}_i) = (1 - y_d) \hat{f}(\mathbf{C}_{0i}) + y_d \hat{f}(\mathbf{C}_{1i}), \quad (1.15)$$

$$\hat{f}(\mathbf{C}) = (1 - z_d) \hat{f}(\mathbf{C}_0) + z_d \hat{f}(\mathbf{C}_1), \quad (1.16)$$

402 where x_d , y_d , and z_d are given as follows:

$$x_d = \frac{x - x_0}{a}, \quad y_d = \frac{y - y_0}{a}, \quad z_d = \frac{z - z_0}{a}. \quad (1.17)$$

403 We can also write

$$\hat{f}(\mathbf{C}) = \sum_{i,j,k \in \{0,1\}} t_x^i t_y^j t_z^k f(\mathbf{C}_{ijk}), \quad (1.18)$$

$$t_\alpha \stackrel{\text{def}}{=} \begin{pmatrix} t_\alpha^0 \\ t_\alpha^1 \end{pmatrix} = \begin{pmatrix} 1 - \alpha_d \\ \alpha_d \end{pmatrix}, \quad (1.19)$$

404 where $\alpha \in \{x, y, z\}$ is an index. This gives a nice geometric interpretation to the
405 trilinear interpolation as shown in Figure 1.9. From this form and the figure, it
406 is apparent that the final interpolated value does not depend on the order of axes
407 along which we perform linear interpolations (see Figure 1.8). Furthermore, we
408 can write $\hat{f}(\mathbf{C})$ as a polynomial:

$$\hat{f}(\mathbf{C}) = \sum_{\alpha, \beta, \gamma \in \{0,1\}} \sum_{i=0}^{\alpha} \sum_{j=0}^{\beta} \sum_{k=0}^{\gamma} (-1)^{(\alpha-i)+(\beta-j)+(\gamma-k)} f(\mathbf{C}_{ijk}) x_d^\alpha y_d^\beta z_d^\gamma. \quad (1.20)$$

409 We take advantage of this form when generalizing trilinear interpolation to irreg-
410 ular grid in section 3.2.2.

411 Maybe a citation here, although I am not sure it is necessary since it could
412 be considered common knowledge. The last two equations are my own (but I'm
413 not sure that's worth mentioning unless there's a citation).

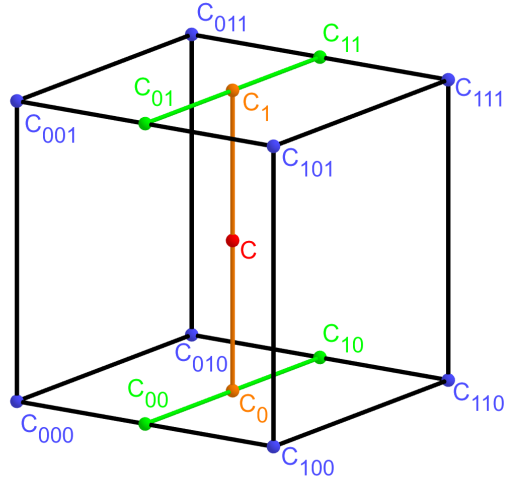


Figure 1.8: Visualization of trilinear interpolation as a composition of linear interpolations (inspired by [27]). We want to interpolate the value in the red point \mathbf{C} . First we interpolate between the four pairs of blue points sharing the last two indices along the x -axis (Eq. 1.14), then between the two pairs of the resulting green points along the y -axis (Eq. 1.15) and finally between the two resulting orange points along the z -axis to get the final red value (Eq. 1.16).

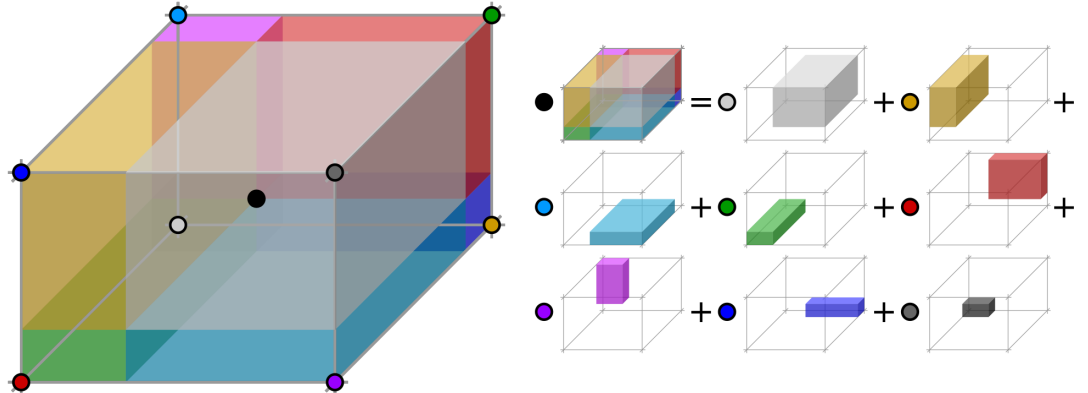


Figure 1.9: Geometric interpretation of trilinear interpolation as expressed in Equation 1.18. The colored dots represent the values in given points and the colored boxes represent the volume in the opposite corner by which the corresponding values are multiplied. The black dot represents the interpolated value which is multiplied by the entire volume [28].

2. Track Simulation

In order to develop and test the reconstruction algorithm, electron and positron tracks are simulated inside the first detector sector \mathcal{D}_1 (see Section 1.3.2) with different initial parameters (origin, initial direction and kinetic energy). Two approaches are currently used to simulate tracks, each of them for different purpose.

The **Microscopic Simulation** uses the Garfield++ toolkit [1]. Within this toolkit:

- a) Magboltz, since it is mentioned later
- b) the High Energy Electro-Dynamics (HEED) program [29] is used to simulate the primary particle,
- c) the class *AvalancheMicroscopic* to simulate the drift of secondary electrons created by ionization in the gas.

This is the most precise and time-consuming simulation used; our current goal is to be able to successfully reconstruct its results and determine our best-case energy resolution.

The **Runge-Kutta Simulation** uses the 4th order Runge-Kutta numerical integration (add citation for Runge-Kutta) to simulate the trajectory of the primary particle in the electromagnetic field inside the detector. It is relatively fast since it does not simulate the secondary particles. It is used as part of our reconstruction algorithm and for testing some parts of the reconstruction.

All of these simulations require the knowledge of the electromagnetic field (both **E** and **B**) inside the detector. A uniform electric field of $400 \text{ V}\cdot\text{cm}^{-1}$ is assumed. The magnetic field was simulated in Maxwell (see Section 1.3.3). add citation

Single track in positive x direction or initial parameter randomization. Importance of gas composition, used gas compositions.

2.1 Microscopic Simulation

The microscopic simulation, the most detailed simulation used in this work, is performed using the Garfield++ toolkit [1].

The electron transport properties are simulated using the program Magboltz (add citation, details?). Two different gas mixtures were compared – 90:10 and 70:30 Ar:CO₂. The second mixture will be used in our detector (this was probably known a priori, but the first tests that I started with used 90/10, so maybe just note that the results justify the fact so far). The temperature is set to 20 °C, the pressure is atmospheric.

The primary track is simulated using the program HEED, which is an implementation of the photo-absorption ionization model [29] (see the reference, moved it to the end of sentence). This program provides the parameters of ionizing collisions. HEED can also be used to simulate the transport of delta electrons; we do not account for these in the current simulation (but plan to include them in the future – maybe mention only in the conclusion/future section). The photons created in the atomic relaxation cascade (fluorescence reabsorption, ?) are also not simulated.

457 Finally, we use the microscopic tracking provided by the class *AvalancheMicroscopic*
 458 in Garfield++ to simulate the drift of the ionization electrons. Each
 459 electron is followed from collision to collision using the equation of motion and
 460 the collision rates calculated by Magboltz.

461 First simulated track in the z direction should be described in detail here (own
 462 subsection of the microscopic section, together with a subsection for random/grid
 463 batches?). Figures.

464 Add more detailed and better description of HEED, and microscopic tracking
 465 (each their own subsection?). Could also mention Monte Carlo (requires gas file
 466 generation - Magboltz) and Runge-Kutta simulation implemented in Garfield,
 467 why we don't use them (another subsection? rename the section to Garfield++
 468 simulation and mention all relevant parts?).

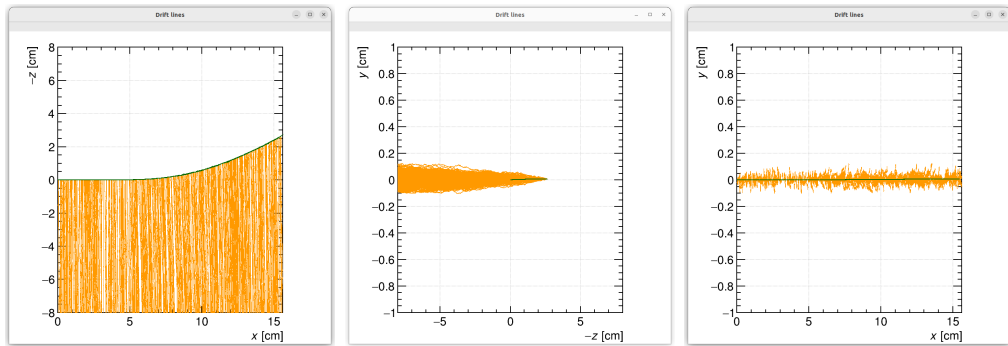


Figure 2.1: Example of a simulated electron track in 70 % argon and 30 % CO₂ atmosphere (on the left). Swap for better images, better zoom. Explain drift lines, primary particle.

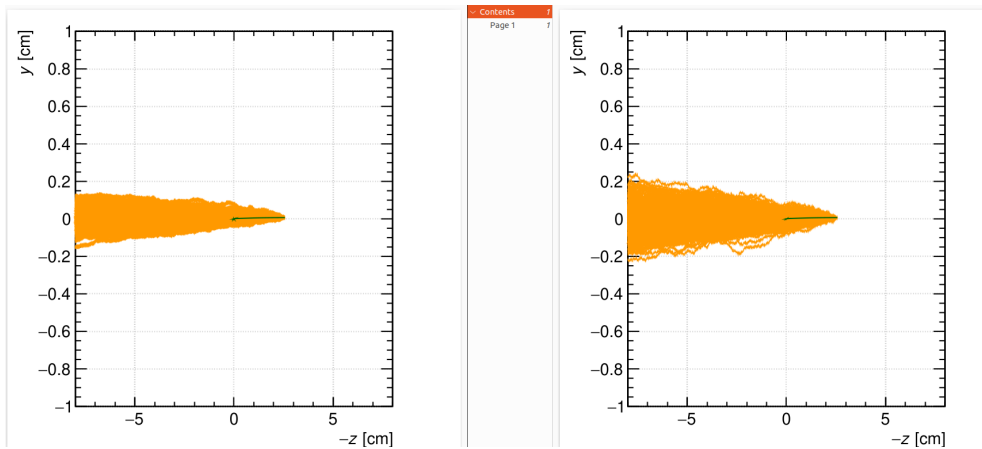


Figure 2.2: Comparison of diffusion in a simulated electron track in 70 % argon, 30 % CO₂ atmosphere and in 90 % argon, 10 % CO₂ atmosphere (on the right). Swap for better image, better zoom. Or put the same pictures for both comparisons in one subfigure, etc. Describe better.

469 2.2 Runge-Kutta Simulation

470 The Runge-Kutta simulation in this work uses the Runge-Kutta 4th order (RK4)
 471 method to numerically integrate the equation of motion of a relativistic charged
 472 particle in an electromagnetic field. Given a system of first order differential
 473 equations

$$\frac{dy}{dt} = \mathbf{f}(t, \mathbf{y}(t)) \quad (2.1)$$

474 with an initial condition

$$\mathbf{y}(t_0) = \mathbf{y}_0, \quad (2.2)$$

475 we iteratively compute the estimate $\mathbf{y}_n = \mathbf{y}(t_n) = \mathbf{y}(t_0 + nh)$ as follows ([citation?](#)
 476 [common knowledge?](#)):

$$\mathbf{k}_1 = \mathbf{f}(t_n, \mathbf{y}_n), \quad (2.3)$$

$$\mathbf{k}_2 = \mathbf{f}\left(t_n + \frac{h}{2}, \mathbf{y}_n + \frac{h\mathbf{k}_1}{2}\right), \quad (2.4)$$

$$\mathbf{k}_3 = \mathbf{f}\left(t_n + \frac{h}{2}, \mathbf{y}_n + \frac{h\mathbf{k}_2}{2}\right), \quad (2.5)$$

$$\mathbf{k}_4 = \mathbf{f}(t_n + h, \mathbf{y}_n + h\mathbf{k}_3), \quad (2.6)$$

$$477 \quad \mathbf{y}_{n+1} = \mathbf{y}_n + \frac{1}{6}(\mathbf{k}_1 + 2\mathbf{k}_2 + 2\mathbf{k}_3 + \mathbf{k}_4). \quad (2.7)$$

478 Alternate forms (infinitely many) possible, accuracy vs computational cost. Runge-
 479 Kutta-Fehlberg with adaptive step size also possible, can potentially save some
 480 computation time especially in rapidly changing field (so maybe not in this case).

481 In our case, we want to integrate the equation of motion, given by the rela-
 482 tivistic Lorentz force:

$$F_L^\mu = m \frac{du^\mu}{d\tau} = q F^{\mu\nu} u_\nu, \quad (2.8)$$

483 where the Einstein summation convention is used, m is the mass of the particle,
 484 q is its charge, u^μ is its four-velocity, τ is the proper time (i.e., time in the particle's
 485 frame of reference) and $F^{\mu\nu}$ is the electromagnetic tensor at given coordinates x^μ
 486 (we consider it to be time-independent in our detector). Given the electric $\mathbf{E} =$
 487 $= (E_x, E_y, E_z)$ and the magnetic field $\mathbf{B} = (B_x, B_y, B_z)$ and using the metric
 488 signature $(+, -, -, -)$, the equation expands to

$$\frac{d}{d\tau} \begin{pmatrix} \gamma c \\ \gamma v_x \\ \gamma v_y \\ \gamma v_z \end{pmatrix} = \frac{q}{m} \begin{pmatrix} 0 & -\frac{E_x}{c} & -\frac{E_y}{c} & -\frac{E_z}{c} \\ \frac{E_x}{c} & 0 & -B_z & B_y \\ \frac{E_y}{c} & B_z & 0 & -B_x \\ \frac{E_z}{c} & -B_y & B_x & 0 \end{pmatrix} \begin{pmatrix} \gamma c \\ \gamma v_x \\ \gamma v_y \\ \gamma v_z \end{pmatrix}, \quad (2.9)$$

489 where c is the speed of light in vacuum, $\mathbf{v} = (v_x, v_y, v_z)$ is the particle's velocity
 490 and $\gamma = (1 - \frac{v^2}{c^2})^{-\frac{1}{2}}$ is the Lorentz factor ([wrong magnetic field sign in the](#)
 491 [implementation???](#)). Together with the equation

$$\frac{d}{d\tau} \begin{pmatrix} ct \\ x \\ y \\ z \end{pmatrix} = \begin{pmatrix} \gamma c \\ \gamma v_x \\ \gamma v_y \\ \gamma v_z \end{pmatrix} = u^\mu, \quad (2.10)$$

492 we get a system of eight first order differential equations for x^μ and u^μ , which
 493 we can integrate using the Runge-Kutta method described above. As a result of
 494 this integration, we get the position $\mathbf{x}(\tau_n)$, the velocity $\mathbf{v}(\tau_n)$ and the detector
 495 time $t(\tau_n)$ for every proper time $\tau_n = n\tau_{\text{step}}$. Integrating using the proper time
 496 means, that the step size in t gets larger by the gamma factor $\frac{dt}{d\tau} = \gamma$ (maybe
 497 change it and integrate the detector time or adjust the step size accordingly). The
 498 only difference is in the step size (because t gets also calculated as it is among
 499 the 8 variables) As initial conditions, we use the origin of the track (x_0, y_0, z_0) ,
 500 the initial velocity direction vector $\mathbf{n} = (\cos \varphi \cos \theta, \sin \varphi \cos \theta, \sin \theta)$ and the ki-
 501 netic energy E_{kin} (initial parameters of the simulation (fit is in chapter 4)), we
 502 then compute γ and $\|\mathbf{v}\|$:

$$\gamma = 1 + \frac{E_{\text{kin}}}{E_0}, \quad (2.11)$$

$$\|\mathbf{v}\| = c\sqrt{1 - \gamma^{-2}}. \quad (2.12)$$

503 Example of RK simulation – first testing track, randomized sample of 100000
 504 tracks.

3. Track Reconstruction

As the first step of the reconstruction algorithm, we reconstruct the track of a primary particle – either an electron or a positron. Then, using this information, we determine the energy of the particle (Section 4).

The **Reconstruction Assuming Steady Drift** uses the standard TPC approach. With parallel fields, the drift inside a uniform electric field remains undistorted (as shown in Equation 1.1). Therefore, we only need to reconstruct the z -coordinate from the drift time using the known drift velocity. We also assume that the readout coordinates (x' , y' , t) are known exactly, neglecting the pads and time binning.

Reconstruction using an **Ionization Electron Map** (from now on referred to as *the map*) uses a simulation of the drift of secondary (ionization) electrons within the detector volume. This simulation can then be used to interpolate the initial position of the secondary electrons. In the first iteration of this method the readout is assumed to be continuous.

We present two algorithms using the map for reconstruction. The first one uses a gradient descent algorithm along with trilinear interpolation (see Section 1.3.3) of the map. The second method uses interpolation on the irregular inverse grid with a polynomial.

The **Discrete Reconstruction** uses the map; instead of reconstructing the exact position of each electron, we reconstruct the center of each hit pad together with the time corresponding to the midpoint of the time bin. The electron count in each TPC bin (consisting of the pad and the time bin) serves as an idealized collected charge, which is then used as a weight in the energy reconstruction fit.

3.1 Reconstruction Assuming Steady Drift

As the first step, we tried to reconstruct an electron track considering a special set of initial parameters. The origin ([starting point?](#)) of the particle is given by the origin of our coordinate system and its initial direction is given by the positive x -axis. This means the magnetic field of our detector is perpendicular to the momentum of the particle at all times, and we can reduce the problem to two-dimensional space. As an example, we use a track simulated using the microscopic simulation with the kinetic energy 8 MeV. The gas composition used in this simulation is 90:10 Ar:CO₂. [Might be better to describe this track in Section 2.1 and reference it here.](#)

For the reconstruction, we decided to use the common method used in a standard TPC ([similar to?](#)). This will allow us to explore the significance of the atypical behavior in our OFTPC. Additionally, we assume the readout is continuous to further simplify the problem. In this approximation, we reconstruct the initial position of each ionization electron.

The reconstruction is then defined by the following relations between the coordinates of the detector space and the readout space (see Section 1.3.2): ([some](#)

546 figure, maybe already relating to some track so that it's not too dull)

$$x = x', \quad (3.1)$$

$$y = y', \quad (3.2)$$

$$z = v_d t, \quad (3.3)$$

547 where v_d is the drift velocity of electrons in the given gas mixture. At a phe-
548 nomenological level, this velocity can be considered as a function of the electric
549 field \mathbf{E} and the magnetic field \mathbf{B} as shown in Equation 1.1. **The Garfield++**
550 **toolkit uses this fact to accelerate their drift simulation with non-microscopic**
551 **approaches (could mention in the simulation chapter).** Since we assume a uni-
552 form electric field in the detector and in this approximation we want to neglect
553 the effect of our unusual magnetic field, we consider the drift velocity constant.
554 **Rewrite this while making figures:** We then approximate this velocity by
555 fitting the dependence $z(t)$ taken from the simulated ionization electrons. This
556 is in one of the provisional figures. Also, this description is not completely ac-
557 curate; in reality, we fit $t1:8-y0$ with $a1*x+a0$ and then invert this and use $8-y0$
558 $= b1*t1+b0$ (old coordinates); $b1=1/a1$ functions as the drift velocity. Maybe
559 also define this $8-z$ variable as an alternative to z in Section 1.3.2 and then use it
560 when correcting this.

561 Later, in a commit after this, I plotted some residues (provisional figure),
562 which could be useful, but for some reason they are residuals from a spline fit of
563 the track?! Probably redo this without the spline fit; just explore the difference
564 in individual points.

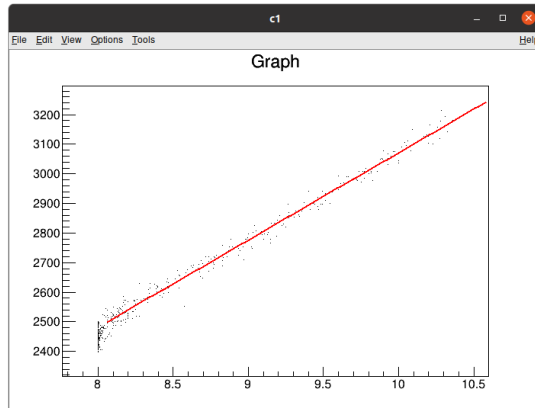


Figure 3.1: Dependence of the drift time on the z coordinate in 90 % argon and 10 % CO_2 atmosphere, fitted with a linear function. The fitted function gives us the average drift velocity in the gas and can be used for rough reconstruction in our TPC. Swap for better image with axis labels, etc. Maybe write the fitted equation.

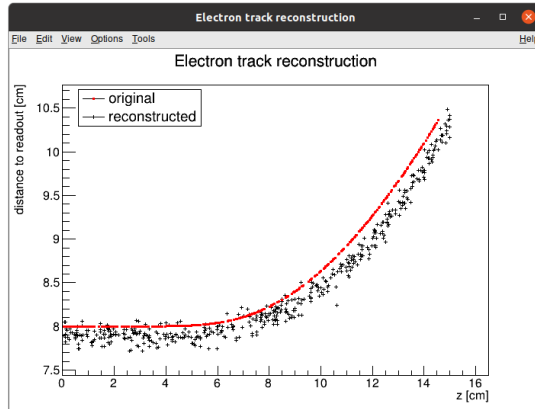


Figure 3.2: The first attempt of a track reconstruction using only the drift velocity. This approach works well in a standard TPC (ideally cite some source). 90 % argon and 10 % CO₂ atmosphere. Swap for better image, correct coordinates.

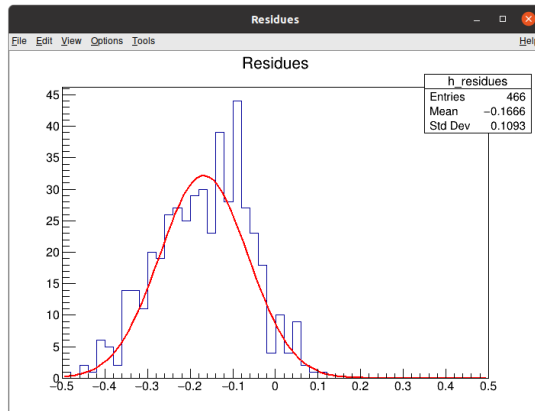


Figure 3.3: First attempt at a track reconstruction using only the drift velocity, residues. Swap for better image, correct coordinates. What's causing the shift? Explain details.

565 3.2 Ionization Electron Map

566 Inside an OFTPC (\exists more than one, also considering it a general concept rather
 567 than the specific OFTPC used at this experiment), the drift of the secondary
 568 (ionization) electrons is significantly affected by its magnetic field (pictures of
 569 the distortion later, the effect is bigger for the 90/10 composition.). We need to
 570 take this into account for accurate reconstruction (should be easy to run the re-
 571 construction without the map and show how much it improves the results). In
 572 the first approximation, we assume a continuous readout (i.e., we neglect the an-
 573 ode segmentation into pads). We can then reconstruct the original position of
 574 each ionization electron using its readout coordinates. For this purpose, we use
 575 the ionization electron map.

576 The ionization electron map represents a mapping from the detector space
 577 to the readout space (see Section 1.3.2). It tells us what readout coordinates

578 (x', y', t) we can expect on average for an ionization electron created at the de-
 579 tector coordinates (x, y, z) . More precisely, it is a mapping to the distributions
 580 on the readout space; we can simplify this as only the means $\bar{\mathcal{M}}$ (**inconsistent**
 581 **notation in the text, write the bar everywhere or nowhere**) and the covariance
 582 matrices \mathcal{M}_{cov} , assuming Gaussian distribution (**test this – some chisq or other**
 583 **statistical test**).

$$\bar{\mathcal{M}} : \mathcal{D} \longrightarrow \mathcal{R}, (x, y, z) \longmapsto (\bar{x}', \bar{y}', \bar{t}). \quad (3.4)$$

584 To get an approximation of this mapping, we simulate the drift of ionization
 585 electrons generated on a regular grid inside the volume of our OFTPC¹. In
 586 order to get accurate results, we use the microscopic simulation of these electrons
 587 described in Section 2.1 (**Monte Carlo from AvalancheMC was also considered**
 588 **but it doesn't (didn't?) include magnetic field, we can probably improve this**
 589 **anyway using the fast track simulation with map proposed in the future section**).
 590 It is also useful to simulate multiple (100 in our case, **this should really only be in**
 591 **a table since there are two map simulations**) electrons originating from the same
 592 position so that we can account for the random fluctuations due to collisions.

593 When evaluating the map inside the grid, we use trilinear interpolation (see
 594 Section 1.3.3). From now on, we will use the same symbol \mathcal{M} for this interpolated
 595 simulation.

596 Finally, we need to invert the map to get the original detector coordinates
 597 (x, y, z) from the given readout coordinates (x', y', t) . In our case, it is reasonable
 598 to assume that the mapping $\bar{\mathcal{M}}$ (**of means (notation inconsistency)**, we lose the
 599 **information about the distribution** (a wild idea how to recover this is in the Future
 600 **section but it will only make sense if the GEM is already accounted for and is**
 601 **very preliminary as there are many factors to consider**) is one-to-one (as seen in
 602 the simulations). We implemented two methods for this purpose: the gradient
 603 descent search (Section 3.2.1) and interpolation on the inverse grid (Section 3.2.2).

604 The simulation (?) of the map is a computationally heavy task. For this rea-
 605 son, we use the MetaCentrum grid [3] to parallelize needed calculations. At first,
 606 this was done by evenly distributing the simulated electrons across the individual
 607 jobs in a simulation with only one electron per vertex in the regular grid with
 608 a spacing of one centimeter. Later, a more efficient approach was implemented,
 609 accounting for the varying lengths of the drift of individual electrons. If we in-
 610 dex the electrons in the order of increasing coordinates y, x, z (**picture will make**
 611 **things clearer**), we can express the number n_l of full XY layers (i.e., electrons
 612 with the same z coordinate) of electrons with index less than or equal to i

$$n_l(i) = \left\lfloor \frac{i}{n_{xy}} \right\rfloor, \quad (3.5)$$

613 where n_{xy} is the number of electrons in each XY layer calculated simply by count-
 614 ing the electrons that satisfy boundary conditions for x and y . **These conditions**
 615 **should be mentioned above; sector condition + maximal x value.** The number of
 616 electrons remaining in the top layer is then

$$n_r(i) = i \bmod n_{xy}. \quad (3.6)$$

¹The detector walls are not considered and we simulate the drift even outside of the OFTPC which allows us to interpolate even close to the walls

617 Finally, we can calculate the sum of the drift gaps of electrons up to index i

$$d_{\text{sum}} = (z_{\max} - z_{\min})n_{xy}n_l - \frac{n_l(n_l - 1)}{2}n_{xy}l + n_r(z_{\max} - z_{\min} - n_l l). \quad (3.7)$$

618 We then use a binary search algorithm to find the maximum index i such that
619 the value of this sum is less than the fraction $\frac{\text{job id}}{\max \text{ job id}}$ of the total sum. This way
620 we obtain the minimal and the maximal index of electrons simulated in the given
621 job. The spacing l should be probably defined above + picture of the simulating
622 grid (1 layer). zmin zmax also

623 After the simulation of the map, we calculate the mean readout coordinates
624 assuming Gaussian distribution (i.e., we use averages). We also calculate standard
625 deviations in a later commit, should be upgraded to the covariance matrix. We
626 never actually plotted the distributions we get when simulating the same electron
627 multiple times, so we do not know if our assumptions are accurate (could also
628 run some statistical test to see how well the Gaussian distribution fits).

629 The obtained map is then stored in a custom class template *Field*, could
630 expand on that. Maybe earlier, since the same template is used for the magnetic
631 field.

632 Could insert a table here describing all 4 simulations of the map (gas composi-
633 tion, spacing, etc.). Simulation inside of one sector (at first double angle). Extra
634 space on the sensor. Edge cases not taken into account (TPC wall). Using qsub
635 (not sure if important). Add plots of distortion of the coordinates. Could also do
636 these plots in a different way (e.g., drawing all the endpoints of each ionization
637 electron or some error ellipse plot).

638

639 Images to add (comparison of both simulations):

- 640 • 3D visualization of the map, simulation example
- 641 • z vs. t plot
- 642 • XY plane distortion for different z values; with arrows and error bars, for
643 all z -layers with different colors
- 644 • XZ plane ($y = 0$) distortion in x (maybe not necessary?)
- 645 • XT plot ($y = 0$) showing (small) distortion in drift times

646

647 More images:

- 648 • Residuals of the continuous readout reconstruction.

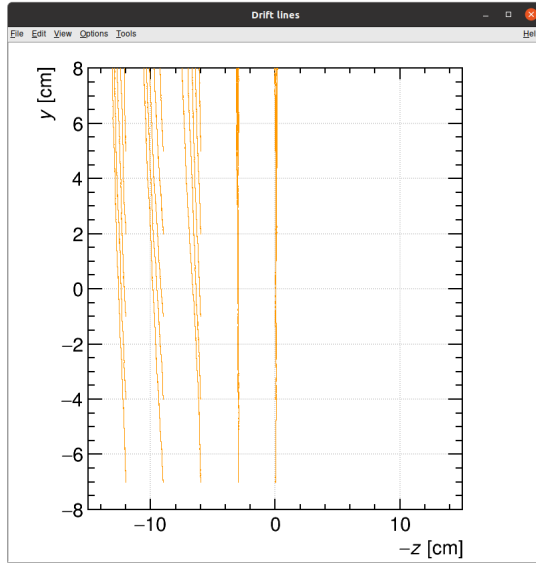


Figure 3.4: Example of map generation. Swap for better image, correct coordinates.

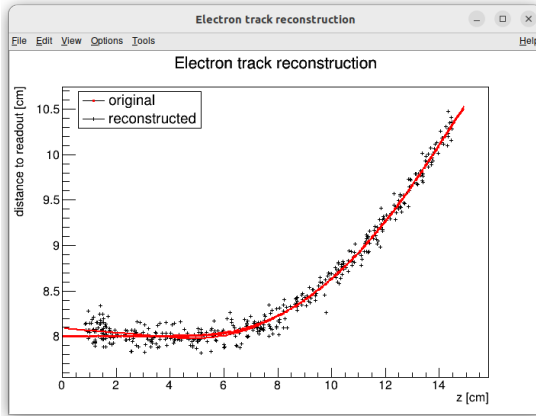


Figure 3.5: Example reconstruction with the map. Swap for better image, correct coordinates.

649 3.2.1 Gradient Descent Algorithm

650 The first implemented method of reconstruction uses a gradient descent algorithm
 651 to calculate an inversion of the map $\bar{\mathcal{M}}$ in a given point. Gradient descent is
 652 an iterative minimization algorithm for multivariate functions. Let $R \in \mathcal{R}$ be
 653 a point in the readout space; we want to find a point $D = (x, y, z) \in \mathcal{D}$ in
 654 the detector space such that

$$\bar{\mathcal{M}}(D) = R = (x'_R, y'_R, t_R). \quad (3.8)$$

655 We define a function f_R in the readout space as a distance in this space:

$$f_R(x', y', t) = \sqrt{(x' - x'_R)^2 + (y' - y'_R)^2 + v_d^2(t - t_R)^2}, \quad (3.9)$$

656 where v_d is an approximation of the drift velocity in the TPC, obtained from
 657 the reconstruction in Section 3.1 (there will be an image with the linear fit here).

658 We make an initial guess (actually in the original code we just take $z = 0$):

$$D_0 = (x'_R, y'_R, v_d t). \quad (3.10)$$

659 Assuming we have the n -th estimate D_n , we calculate the i -th component of
660 the gradient of $f_R \circ \bar{\mathcal{M}}$ numerically using central differences: (signs look correct)

$$[\nabla(f_R \circ \bar{\mathcal{M}})]^i(D_n) \approx \frac{f_R(\bar{\mathcal{M}}(D_n + s \cdot e^i)) - f_R(\bar{\mathcal{M}}(D_n - s \cdot e^i))}{2s}, \quad (3.11)$$

661 where $e^i \in \mathcal{D}$ is the i -th coordinate vector and s is the step size. The step size
662 should be sufficiently small; initially, we set it as a fraction $s = \frac{l}{10}$ of the map's
663 grid spacing l . During the minimization, we check that $f_R(\bar{\mathcal{M}}(D_n)) < 10s$ at all
664 times (s can (?) change – check). When using trilinear interpolation, it would be
665 more efficient to calculate the gradient explicitly (\pm same result). This could be
666 implemented inside the *Field* template class. The next iteration can be calculated
667 as follows:

$$D_{n+1} = D_n - \gamma \nabla(f_R \circ \bar{\mathcal{M}})(D_n), \quad (3.12)$$

668 where $\gamma \in \mathbb{R}^+$ is the damping coefficient. It should be set to a small enough
669 value to ensure convergence, but large enough for sufficient converging speed.
670 The minimization stops either when the error $f_R(\bar{\mathcal{M}}(D_n))$ drops below a specified
671 value or when the number of iterations exceeds a certain limit (in this case,
672 a message is printed into the console). The parameters of this method can be
673 further optimized (e.g., a better choice of γ , gradient computation); instead, we
674 later decided to use the interpolation on the inverse grid described in the next
675 section.

676 Measure reconstruction duration and compare it with the inverse grid inter-
677 polation? Also compare the result? Typical evolution of D_n during search. Not
678 sure if this has to be cited.

679 3.2.2 Interpolation on the Inverse Grid

680 Interpolation should be generally faster than the gradient descent since we don't
681 need to iterate. We also don't need to optimize it to improve performance, if
682 it's too slow we can even calculate the coefficients for the entire map before
683 reconstruction (again, do some profiling).

684 The best current algorithm uses the interpolation on the inverse grid. Rather
685 than inverting the trilinearly interpolated map using a numerical minimization
686 method as in the previous section, we take advantage of the fact that the map
687 $\bar{\mathcal{M}}$ is one-to-one (isomorphism is supposed to preserve structure, not sure how
688 to interpret that here, not the best description, we already (kind of) assume it
689 is a bijection by saying we will invert it). Since we have simulated values of this
690 map on a regular grid in the detector space \mathcal{D} , we also know the inverse map $\bar{\mathcal{M}}^{-1}$
691 on the irregular inverse grid in the readout space \mathcal{R} . To get an approximation
692 of the inverse map in the entire readout space, we can use interpolation (general
693 concept, the specific choice is described below).

694 Since the inverse grid is irregular, trilinear interpolation cannot be applied.
695 Given that the simulated map is dense enough to provide a good approximation

696 considering the size of our pads, we can adopt a similar approach.² As shown in
 697 Equation 1.20 in Section 1.3.3, trilinear interpolation (**shouldn't need an article**
 698 **when talking about a general concept**) can be expressed as a polynomial:

$$\hat{f}(x, y, z) = axyz + bxy + cxz + dyz + ex + fy + gz + h, \quad (3.13)$$

699 where a, b, c, d, e, f, g, h are coefficients uniquely determined by the values of
 700 the function at the vertices of the interpolation cell (**can be calculated in the**
 701 **way shown in the mentioned equation, not sure what more to add**). We can gen-
 702 eralize this for a function defined on an irregular grid. Given the function values
 703 at any eight points, we can write a system of eight linear equations

$$\begin{pmatrix} x_1y_1z_1 & x_1y_1 & x_1z_1 & y_1z_1 & x_1 & y_1 & z_1 & 1 \\ \vdots & \vdots \\ x_8y_8z_8 & x_8y_8 & x_8z_8 & y_8z_8 & x_8 & y_8 & z_8 & 1 \end{pmatrix} \begin{pmatrix} a \\ \vdots \\ h \end{pmatrix} = \begin{pmatrix} f(x_1, y_1, z_1) \\ \vdots \\ f(x_8, y_8, z_8) \end{pmatrix}, \quad (3.14)$$

704 which has a unique solution for the coefficients for most values of (x_n, y_n, z_n) and
 705 $f(x_n, y_n, z_n)$, where $n \in \{1, \dots, 8\}$.

706 This approach introduces a small complication: finding the correct pseudocell
 707 (i.e., the image of eight vertices forming a cubic cell in the regular grid) in
 708 the inverse grid. The eight irregularly spaced vertices of this pseudocell do not
 709 define a unique volume, so there are multiple possible ways to partition \mathcal{R} into
 710 pseudocells, with no obvious choice among them.

711 We are currently ignoring this problem and performing binary search along
 712 x, y, z (in this order). It shouldn't matter too much because the 70/30 map
 713 doesn't cause such a big distortion and was even accidentally extrapolated for all
 714 z different from the central plane.

²A more complicated and computationally heavy alternative would be natural neighbor interpolation or Kriging.

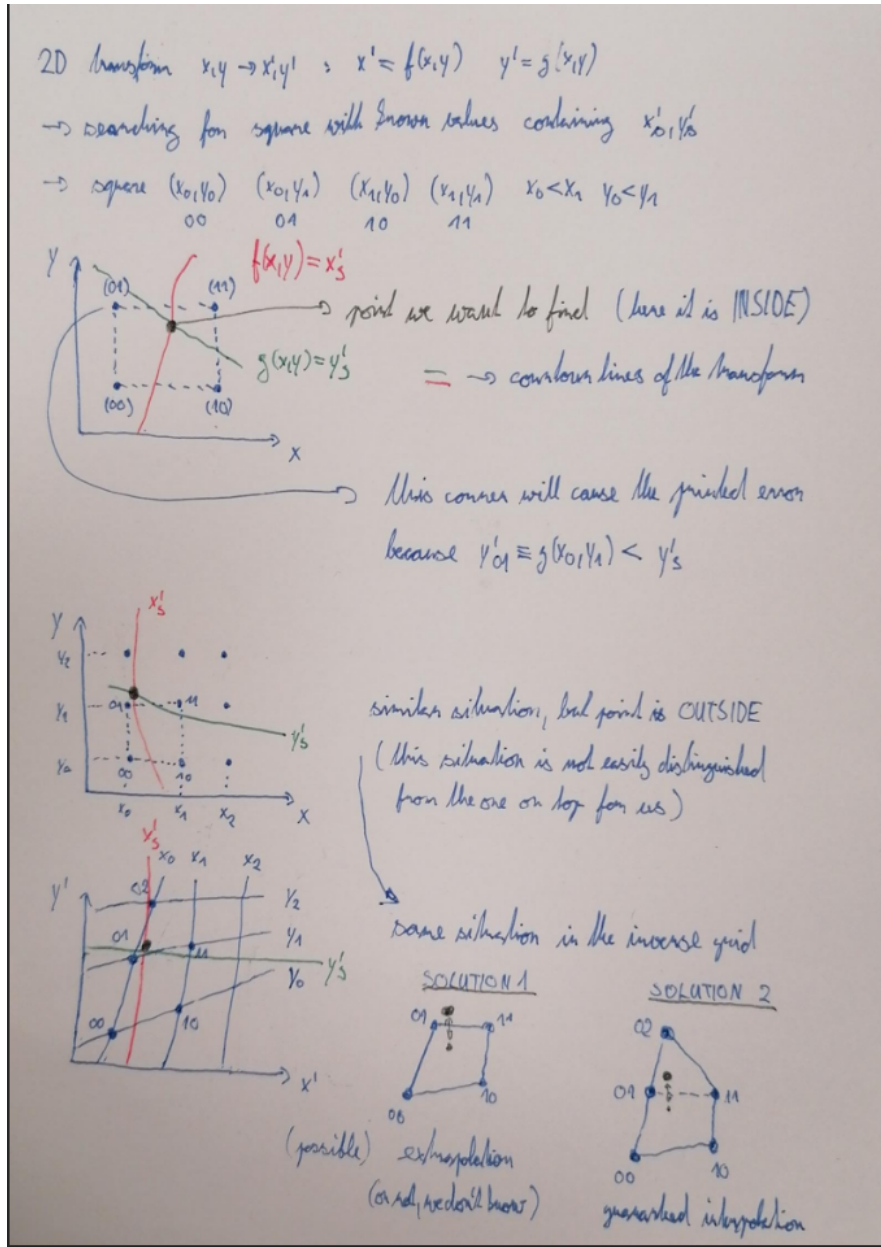


Figure 3.6: Selection of the points for interpolation. Create better images; use the explanation interpolation vs. extrapolation strange property. Solution 2 probably does not make much sense.

715 3.3 Discrete Reconstruction

716 Reconstruction with pads and time bins. Maybe testing different pads.

717 It is also possible to make this a subsection of the map, making the previous
718 subsections parts of a new subsection 'Map Inversion'.

719 In order to get a more realistic representation of a track measured in the OFTPC,
720 we need to take the discretization of the position and time data into account.
721 The readout of the OFTPC will consist of 128 pads, their layout is shown in
722 Figure 1.6. Time is read out in discrete bins of size $t_{\text{bin}} = 100$ ns.

723 As the first approximation, we can neglect the multiplication in the triple-GEM.

724 and assume an ideal charge readout. The time measurement starts at the begin-
 725 ning of the electron/positron simulation (depending on the specific simulation it
 726 can correspond to the production in the target or when entering the OFTPC,
 727 here the specific time doesn't matter too much since the primary particle trav-
 728 els basically at light speed (30 ps/cm) which is circa immediate given the time
 729 binning). Randomize this time a bit and see what it does to the reconstruction.
 730 The readout coordinates $(x', y', t) \in \mathcal{R}$ of each ionization electron can be mapped
 731 to the pad coordinates $(n_{\text{pad}}, n_t) \in \mathcal{P}$:

$$n_{\text{pad}} = n: (x', y') \in \left[x_{1,n} - \frac{g}{2}, x_{2,n} + \frac{g}{2} \right] \times \left[y_{1,n} - \frac{g}{2}, y_{2,n} + \frac{g}{2} \right], \quad (3.15)$$

$$n_t = \left\lceil \frac{t}{t_{\text{bin}}} \right\rceil, \quad (3.16)$$

732 where $x, y_{1,n}$ and $x, y_{2,n}$ are the opposing pad corner coordinates, and g is the
 733 gap between the pads (described in detail in Section 1.3.2). This way, the closest
 734 pad is assigned to each readout position within the OFTPC volume³. Makes
 735 sense since the pads attract the electrons, the inhomogeneity of electric field is
 736 neglected. The number of electrons collected by each pad (i.e., collected charge)
 737 in each time bin is then counted and serves as a weight for the energy recon-
 738 struction. The reconstructed track consists of points for each $(n, n_t) \in \mathcal{P}$, we get
 739 these by reconstructing the position of a hypothetical electron with the readout
 740 coordinates of the pad/time bin center:⁴

$$\mathcal{D} \ni (x, y, z) = \overline{\mathcal{M}} \left(x_{c,n}, y_{c,n}, \left(n_t - \frac{1}{2} \right) t_{\text{bin}} \right). \quad (3.17)$$

³Some positions near the wall are not handled and some pads extend beyond the OFTPC volume. This is where an electric field simulation would come in handy.

⁴Mapping the center of the pad (along with the midpoint of the time bin) isn't necessarily the best approach since it might not correspond to the average parameters of an electron with these readout parameters.

741 4. Energy Reconstruction

742 The second stage is the reconstruction of the particle's energy using a fit of its
743 reconstructed track (see Section 3). We have tested three ways of reconstructing
744 the energy. Fitting is done using the MINUIT algorithm implemented in
745 ROOT [2]. Cite some CERN article directly on MINUIT, can add a section. Or
746 is it done using MIGRAD? The circle and RK4 probably was.

747 The **Cubic Spline Fit** was a tested and later rejected method of energy reconstruction.
748 It uses smoothly connected piecewise cubic polynomials between uniformly spaced nodes.
749 The reconstructed energy is calculated using the fit parameters by computing the radius of curvature in different points of the fitted
750 curve using the known magnitude of the magnetic field perpendicular to the trajectory.
751 We rejected this method because the tuning of the fit turned out to be unpractical compared to the other used methods.
752 Reconstructs energy at every position (even though the actual energy doesn't change much) and it might be
753 slower but no profiling has been done yet. Of course, it wasn't tested on the
754 newer track reconstruction methods at all.

755 The **Circle and Lines Fit** was chosen as an alternative since this corresponds to the shape of a trajectory of a charged particle crossing a finite volume
756 with a homogeneous magnetic field. The energy of the particle can be estimated
757 using the fitted radius and the magnitude of the perpendicular magnetic field in
758 the middle of the TPC.

759 The **Runge-Kutta Fit** uses the 4th order Runge-Kutta numerical integration
760 described in Section 2.2. Initial parameters of the track (including the particle's
761 energy) are optimized so that the integrated trajectory fits to the reconstructed
762 one. This fit can also be performed as a single parameter (i.e., energy) fit if we
763 get the initial position and orientation of the particle on the entrance to the TPC
764 from previous detectors (TPX3 and MWPC, see Section 0.2).

768 4.1 Cubic Spline Fit

769 The first attempt to get an estimate of the kinetic energy of the particle uses
770 a cubic spline fit. We use an electron track starting in the origin of our coordinate

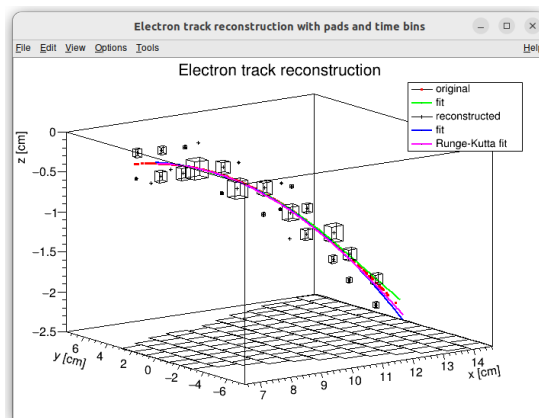


Figure 4.1: Example of a fitted reconstructed track. Swap for better image.

771 system with an initial direction in the positive x axis. The example track is
 772 simulated microscopically (see Section 2.1) with a kinetic energy of 8 MeV in
 773 a gas mixture 90% Ar + 10% CO₂ (the same track was used in Section 3.1). **This**
 774 **track should probably be described in the simulation chapter.**

775 In order to calculate the spline, we use the class *TSplines3* from ROOT. This
 776 allows us to evaluate the spline using the coordinates (x_n, z_n) of each node and
 777 the derivatives d_1, d_2 in the first and the last node. We can fit these parameters
 778 of a fixed amount of nodes to the simulated trajectory. We use the IMPROVE
 779 algorithm provided by the *TMinuit* class in ROOT (**there are some guidelines for**
 780 **fonts in MFF UK template (Czech version) that I will eventually apply (see notes**
 781 **in the conclusion)**). This algorithm attempts to find a better local minimum after
 782 converging (**could reformulate a bit, taken word for word from some manual**).

783 After the fit converges, we calculate an energy estimate using the radius of
 784 curvature, which we can extract from the fitted spline equation at every point of
 785 the trajectory. The part of the spline corresponding to a given node is defined as

$$z(x) = z_n + b\Delta x + c(\Delta x)^2 + d(\Delta x)^3, \quad (4.1)$$

786 where $\Delta x = x - x_n$ and b, c, d are coefficients. Using this equation, we derive
 787 the radius of curvature¹ as:

$$r(x) = \frac{(1 + z'^2(x))^{\frac{3}{2}}}{z''(x)} = \frac{(1 + (b + 2c\Delta x + 3d(\Delta x)^2)^2)^{\frac{3}{2}}}{2c + 6d\Delta x}. \quad (4.2)$$

788 Based on the geometry of our detector, we assume that the magnetic field satisfies
 789 $\mathbf{B}(x, 0, z) = (0, B(x, z), 0)$ for a track in the XZ plane. Since the electron is rela-
 790 tivistic, the effect of the electric field on its trajectory is negligible. The Lorentz
 791 force F_L is then always perpendicular to the momentum of the electron and acts
 792 as a centripetal force F_c (**not quite sure how to handle this then?**):

$$\begin{aligned} \mathbf{F}_L &= \mathbf{F}_c, \\ \|e\mathbf{v} \times \mathbf{B}\| &= \frac{\gamma m_e v^2}{r}, \\ ec\beta B &= \frac{E_{0e}\beta^2}{r\sqrt{1 - \beta^2}}, \end{aligned} \quad (4.3)$$

$$\begin{aligned} \sqrt{1 - \beta^2} &= \frac{E_{0e}\beta}{ecBr}, \\ \beta^2(x) &= \left[1 + \left(\frac{E_{0e}}{ecB(x, z(x))r(x)}\right)^2\right]^{-1}, \end{aligned} \quad (4.4)$$

793 where e is the elementary charge, c is the speed of light in vacuum, m_e is the rest
 794 mass of electron, $E_{0e} = m_e c^2$ is its rest energy, γ is the Lorentz factor, \mathbf{v} is
 795 the velocity of the electron, and $\beta = \frac{v}{c}$. The kinetic energy for a given point on
 796 the trajectory is then given as

$$E_{\text{kin}}(x) = \left(\frac{1}{\sqrt{1 - \beta^2(x)}} - 1\right) E_{0e}. \quad (4.5)$$

¹For the general formula see https://en.wikipedia.org/wiki/Curvature#Graph_of_a_function.

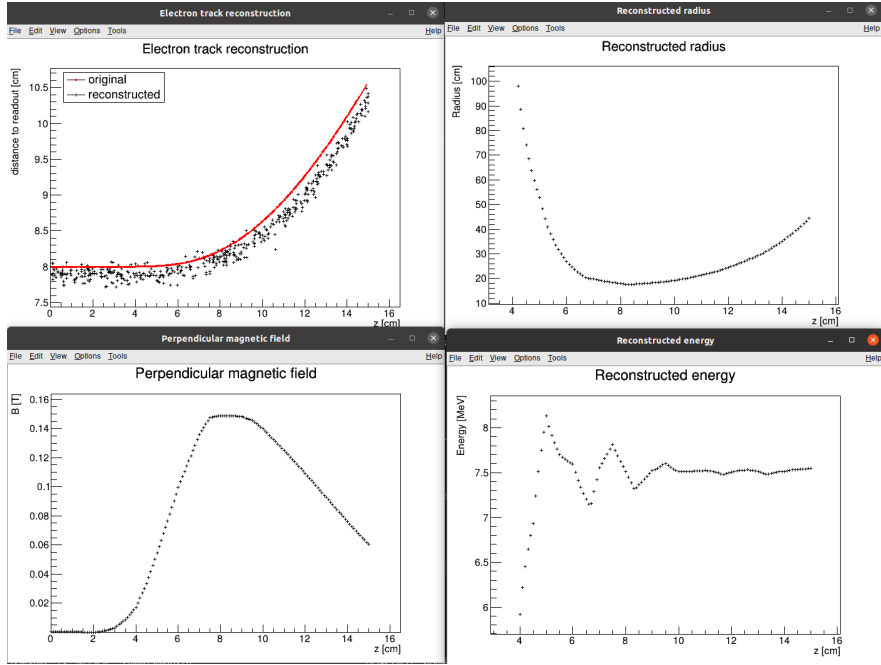


Figure 4.2: First attempt at a track reconstruction using only the drift velocity. Spline energy reconstruction attempt. Swap for better image(s) – subfigure environment, correct coordinates.

797 We can then average these estimates at multiple points (possibly using some
 798 weights to account for the change in accuracy, this wasn't optimized and we just
 799 ended with the graph) to get a single value. This method was later rejected in
 800 favor of the circle and lines fit the name was already established at the beginning
 801 of the chapter described in the next section. Add some figures.

802 4.2 Circle and Lines Fit

803 Another way to estimate the particle's kinetic energy is to fit its (??) trajectory
 804 with a circular arc with lines attached smoothly. This shape of trajectory cor-
 805 responds to a movement of a charged particle through a homogeneous magnetic
 806 field perpendicular to the particle's momentum and limited to a certain volume.
 807 In general, the shape of such a trajectory with a non-perpendicularly oriented
 808 momentum is a spiral. In our case, the magnetic field is approximately toroidal
 809 and the particle motion is nearly perpendicular to it (verify, could add some
 810 magnetic field plots in different vertical planes; shouldn't have a big effect on the
 811 reconstructed radius anyway). At first, we tested a 2D version of this fit, then
 812 we adapted it to 3D.

813 The field in our detector is not homogeneous, it is therefore not entirely clear
 814 what value of magnetic field should be used along with the fitted radius (using
 815 equations 4.4 and 4.5) to get the best estimate for the kinetic energy. Since we
 816 only use this method as the first iteration of the particle's energy that we later
 817 refine, an optimal solution of this problem is not required. Instead, we tested two
 818 options: taking the value of the field in the middle of the fitted circular arc (or
 819 is it in the middle x of the OFTPC?) and taking the average field along it. We

haven't really tried to plot this for multiple tracks, but these estimates are saved somewhere and could be plotted.

4.2.1 Two-dimensional fit

In the 2D case, the fitted function used for the electron track² described in Section 4.1 (or in microsim? one specific track at the time, technically this function doesn't work for a curvature that gets outside of the semicircle) is defined as follows: Maybe describe this track that we used at the beginning somewhere earlier (section microscopic simulations → Testing track?) so that it is easier to refer to it in multiple sections. It is not part of the early GitHub commits, so maybe it won't be possible to create exact replicas of the images, but they should be at least very similar.

$$z(x) = \begin{cases} a_1x + b_1 & x < x_1 \\ z_0 + \sqrt{r^2 - (x - x_0)^2} & x_1 \leq x \leq x_2 \\ a_2x + b_2 & x > x_2 \end{cases}, \quad (4.6)$$

where $a_{1,2}$ and $b_{1,2}$ are the parameters of the lines, (x_0, z_0) is the center of the circle, r is its radius, and $(x_{1,2}, z_{1,2})$ are the coordinates of the function's nodes. That means we have 9 parameters ($z_{1,2}$ are not used in the function) along with 2 continuity conditions and 2 smoothness conditions (9 parameters of the described function, 5 of them independent after taking the conditions into account). For the fit, we use the coordinates of the nodes and the radius of the circle, which gives us 5 independent parameters (only the radius has to be larger than half of the distance between nodes). The continuity conditions (combined with the relations for $z_{1,2}$) are

$$z_{1,2} = a_{1,2}x_{1,2} + b_{1,2} = z_0 - \sqrt{r^2 - (x_{1,2} - x_0)^2}, \quad (4.7)$$

the smoothness conditions are

$$a_{1,2} = \frac{x_0 - x_{1,2}}{\sqrt{r^2 - (x_{1,2} - x_0)^2}}. \quad (4.8)$$

Together with the Equation 4.7 we get the values of $b_{1,2}$

$$b_{1,2} = z_{1,2} - a_{1,2}x_{1,2}. \quad (4.9)$$

For the coordinates of the center of the circle, we can use the fact that the center has to lie on the axis of its chord. In other words, there is a value of a parameter t such that, using the parametric equation of the axis

$$\begin{pmatrix} x_0 \\ z_0 \end{pmatrix} = \begin{pmatrix} \frac{x_1+x_2}{2} \\ \frac{z_1+z_2}{2} \end{pmatrix} + t \begin{pmatrix} \frac{z_2-z_1}{2} \\ \frac{x_1-x_2}{2} \end{pmatrix}. \quad (4.10)$$

At the same time, the center has to be in a distance of r from the nodes:

$$\begin{aligned} (x_1 - x_0)^2 + (z_1 - z_0)^2 &= r^2, \\ \left(\frac{x_1 - x_2}{2} + \frac{z_1 - z_2}{2}t \right)^2 + \left(\frac{z_1 - z_2}{2} + \frac{x_2 - x_1}{2}t \right)^2 &= r^2, \\ \left(\left(\frac{x_2 - x_1}{2} \right)^2 + \left(\frac{z_2 - z_1}{2} \right)^2 \right)t^2 + \left(\frac{x_2 - x_1}{2} \right)^2 + \left(\frac{z_2 - z_1}{2} \right)^2 - r^2 &= 0. \end{aligned} \quad (4.11)$$

²Electron tracks bend towards negative z , we need to use the upper part of the circle

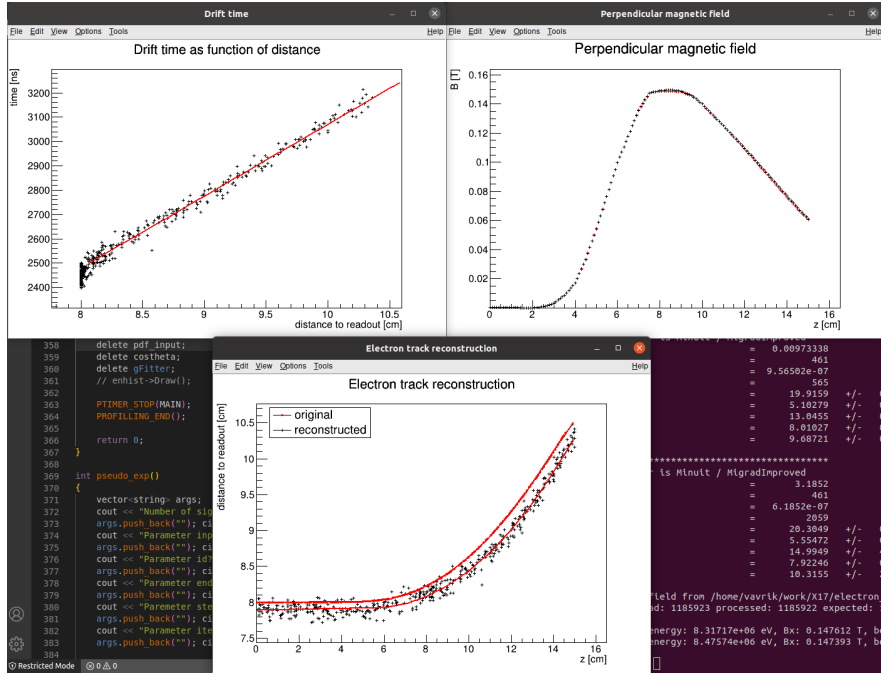


Figure 4.3: First attempt at a track reconstruction using only the drift velocity. Circle and Lines Fit in 2D. Swap for better image, correct coordinates. Bias should be described in the previous chapter, not here.

846 Since our electron track bends towards negative z and $x_2 > x_1$, we only care
847 about the solution with $t > 0$

$$t = \sqrt{\frac{r^2}{\left(\frac{x_2-x_1}{2}\right)^2 + \left(\frac{z_2-z_1}{2}\right)^2} - 1}, \quad (4.12)$$

$$x_0 = \frac{x_1 + x_2}{2} + \frac{z_2 - z_1}{2} \sqrt{\frac{r^2}{\left(\frac{x_2-x_1}{2}\right)^2 + \left(\frac{z_2-z_1}{2}\right)^2} - 1}, \quad (4.13)$$

$$z_0 = \frac{z_1 + z_2}{2} - \frac{x_2 - x_1}{2} \sqrt{\frac{r^2}{\left(\frac{x_2-x_1}{2}\right)^2 + \left(\frac{z_2-z_1}{2}\right)^2} - 1}.$$

848 The function defined in Equation 4.6 along with equations 4.8, 4.9, and 4.13
849 derived using the continuity and smoothness conditions (combined with the re-
850 lations for $z_{1,2}$) fully define our fitted function with parameters $r, x_{1,2}, z_{1,2}$. Some
851 pictures of the fit on the tested track. Results of the fit. Again, the actual fit
852 uses 8-z. Use GeoGebra schematics to generate a picture of 2D geometry.

853 4.2.2 Three-dimensional fit

854 Explain the geometry and least square method used for the 3D fit. Tested on
855 a Runge-Kutta sample, and with microscopic tracks + map simulation.

856 In three dimensions, the shape of a trajectory of a charged particle in a uniform
857 magnetic field is a cylindrical helix. Nevertheless, since we assume that the
858 field is approximately perpendicular to the particle's momentum at all times, we

will further approximate the trajectory with a circular arc (with lines attached smoothly).

We assume that the initial position $\mathbf{X}_0 = (x_0, y_0, z_0)$ and direction θ, φ (spherical angles as in Section 1.3.2) are known, since this information will be provided by TPX3 and MWPC layers. We could further refine it at the end of the current algorithm with some kind of global fit (all detector layers). The fit then has four free parameters (figure):

- the length of the first line l (as measured from the initial position),
- the radius of the circular arc r ,
- the central angle of the arc $\phi_{\max} \in [0, 2\pi]$,
- the direction of the curvature given by the angle $\alpha \in [0, 2\pi]$ (right-handed with respect to the particle direction, $\alpha = 0$ if the particle curves towards negative z in a plane given by $\hat{\mathbf{z}}$ and the direction vector).

Using these parameters, we can derive a parametrization of the whole curve. Let \mathbf{v} be the initial unit direction vector, i.e., using the spherical angles

$$\mathbf{v} = (\cos \varphi \cos \theta, \sin \varphi \cos \theta, \sin \theta)^T, \quad (4.14)$$

then we can parameterize the first line as follows:

$$\mathbf{X}_{L1}(t) = \mathbf{X}_0 + t\mathbf{v} \quad t \in [0, l]. \quad (4.15)$$

This gives us the starting point of the arc

$$\mathbf{X}_1 = \mathbf{X}_{L1}(l) = \mathbf{X}_0 + l\mathbf{v}. \quad (4.16)$$

The vector \mathbf{c}_1 that lies in the plane of curvature and points from \mathbf{X}_1 to the center of curvature can be calculated using a composition of rotations. First, we rotate \mathbf{v} to point in the $\hat{\mathbf{x}}$ direction, the normal for $\alpha = 0$ than points in the $-\hat{\mathbf{z}}$ direction, we apply the α rotation and reverse the rotations into the $\hat{\mathbf{x}}$ direction: (parameters are explained in the bullet points above)

$$\begin{aligned} \mathbf{c}_1 &= R_z(\varphi)R_y(-\theta)R_x(\alpha)R_y\left(\frac{\pi}{2}\right)R_y(\theta)R_z(-\varphi)\mathbf{v}, \\ &= R_z(\varphi)R_y(-\theta)R_x(\alpha)(-\hat{\mathbf{z}}), \\ &= \begin{pmatrix} \cos \varphi & -\sin \varphi & 0 \\ \sin \varphi & \cos \varphi & 0 \\ 0 & 0 & 1 \end{pmatrix} \begin{pmatrix} \cos \theta & 0 & -\sin \theta \\ 0 & 1 & 0 \\ \sin \theta & 0 & \cos \theta \end{pmatrix} \begin{pmatrix} 1 & 0 & 0 \\ 0 & \cos \alpha & -\sin \alpha \\ 0 & \sin \alpha & \cos \alpha \end{pmatrix} \begin{pmatrix} 0 \\ 0 \\ -1 \end{pmatrix}, \quad (4.17) \\ &= \begin{pmatrix} -\sin \alpha \sin \varphi + \cos \alpha \cos \varphi \sin \theta \\ \sin \alpha \cos \varphi + \cos \alpha \sin \varphi \sin \theta \\ -\cos \alpha \cos \theta \end{pmatrix}. \end{aligned}$$

Signs should be correct because right-handed rotation around y rotates z into x and this one is the opposite. Seems like in this part of the code θ is actually taken from the pole. Instead of the equator plane. Similarly by rotating $\hat{\mathbf{y}}$, we can get the normal vector $\mathbf{n} = \mathbf{v} \times \mathbf{c}_1$ perpendicular to the plane of the trajectory:

$$\mathbf{n} = R_z(\varphi)R_y(-\theta)R_x(\alpha)\hat{\mathbf{y}} = \begin{pmatrix} -\cos \alpha \sin \varphi - \sin \alpha \cos \varphi \sin \theta \\ \cos \alpha \cos \varphi - \sin \alpha \sin \varphi \sin \theta \\ \sin \alpha \cos \theta \end{pmatrix}. \quad (4.18)$$

885 This allows us to express the coordinates of the center \mathbf{C} of the circular arc:

$$\mathbf{C} = \mathbf{X}_1 + r\mathbf{c}_1. \quad (4.19)$$

886 We can then get the parametrization and the endpoint of the circular arc using
887 Rodrigues' rotation formula: (all parameters explained in the bullet points above)

$$\begin{aligned} \mathbf{c}_2 &= \mathbf{c}_1 \cos \phi_{\max} + (\mathbf{n} \times \mathbf{c}_1) \sin \phi_{\max} + \mathbf{n}(\mathbf{n} \cdot \mathbf{c}_1)(1 - \cos \phi_{\max}), \\ &= \mathbf{c}_1 \cos \phi_{\max} - \mathbf{v} \sin \phi_{\max}, \end{aligned} \quad (4.20)$$

$$\mathbf{X}_C(\phi) = \mathbf{C} - r(\mathbf{c}_1 \cos \phi - \mathbf{v} \sin \phi) \quad \phi \in [0, \phi_{\max}], \quad (4.21)$$

$$\mathbf{X}_2 = \mathbf{X}_C(\phi_{\max}) = \mathbf{C} - r\mathbf{c}_2, \quad (4.22)$$

888 and if we define the direction vector of the second line, we also get its parametriza-
889 tion

$$\mathbf{w} = \mathbf{v} \cos \phi_{\max} + (\mathbf{n} \times \mathbf{v}) \sin \phi_{\max} = \mathbf{v} \cos \phi_{\max} + \mathbf{c}_1 \sin \phi_{\max}, \quad (4.23)$$

$$\mathbf{X}_{L2}(s) = \mathbf{X}_2 + s\mathbf{w} \quad s \in [0, \infty). \quad (4.24)$$

890 The fit is performed as a (weighted) least square minimization (**MIGRAD**
891 **ROOT**), therefore we need to derive the distance of any point \mathbf{P} to the fitted
892 curve. For the first line, we simply compute the parameter value of the closest
893 point on the line:

$$\begin{aligned} t_P &= \mathbf{v} \cdot (\mathbf{P} - \mathbf{X}_1), \\ d_{P1} &= \|\mathbf{P} - \mathbf{X}_{L1}(t_P)\|. \end{aligned} \quad (4.25)$$

894 If the parameter value is outside of its bounds defined above, we take the bound-
895 ary value instead. The distance to the second line is computed likewise. For
896 the circular arc (specific circular arc in the fit), we find the closest point (on the
897 arc) by projecting the center connecting line onto the arc plane:

$$\mathbf{X}_{PC} = \mathbf{X}_C + r \frac{(\mathbf{P} - \mathbf{X}_C) - (\mathbf{n} \cdot (\mathbf{P} - \mathbf{X}_C))\mathbf{n}}{\|(\mathbf{P} - \mathbf{X}_C) - (\mathbf{n} \cdot (\mathbf{P} - \mathbf{X}_C))\mathbf{n}\|}, \quad (4.26)$$

$$d_{PC} = \|\mathbf{P} - \mathbf{X}_{PC}\| \quad (4.27)$$

898 Potential problem in the implementation – might not be correctly handling ϕ
899 out of bounds, the distance could be sometimes underestimated because of this.

900 The shortest distance out of d_{P1}, d_{PC}, d_{P2} is then taken as the distance to the curve.
901 When calculating energy with the average field, only the arc is considered. Mid-
902 dle field in the current implementation taken in the middle x plane (intersection
903 with the curve). TVirtualFitter+MIGRAD, maximal num of iterations, tolera-
904 tion. Different uncertainties in x, y, z not taken into account.

905 4.3 Runge-Kutta Fit

906 The Runge-Kutta fit uses the Runge-Kutta 4th order (RK4) numerical integra-
907 tion of the equation of motion (see Section 2.2) to find the best values of the track
908 parameters – the track origin, initial velocity direction and the kinetic energy. In
909 order to speed up the energy reconstruction, an initial guess of these parameters
910 can be obtained from the 3D circle fit described in the previous section. Fur-
911 thermore, assuming we know the track origin and orientation, we can perform

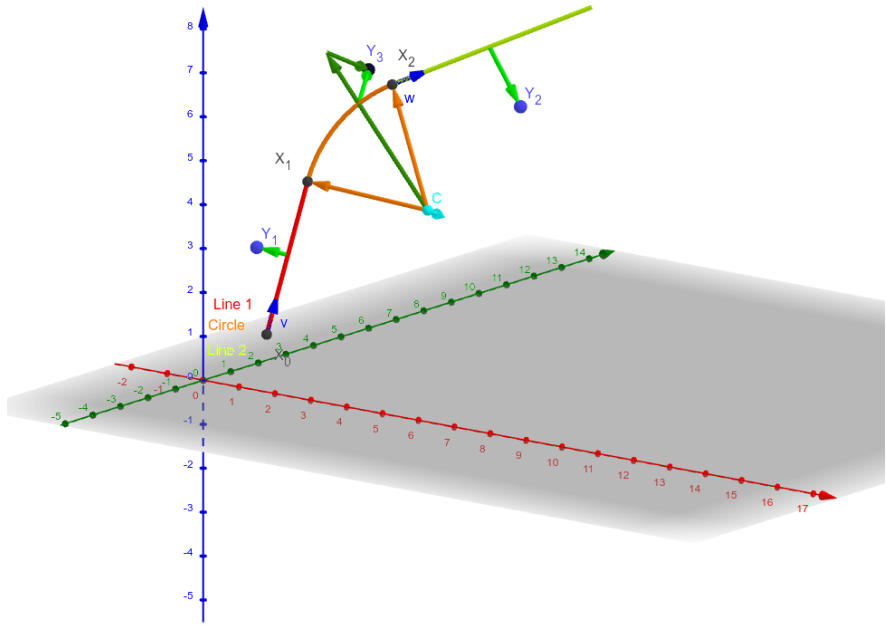


Figure 4.4: Circle and Lines Fit 3D geometry. Swap for better image.

912 a single parameter fit of the kinetic energy (**do some profiling and show that it is**
 913 **faster – below in the microscopic testing**).

914 The fit is performed as a least square minimization of the (weighted) distances
 915 of the track points (true ionization vertices from the simulation or reconstructed
 916 points). The simulated RK4 track consists of line segments with known endpoints,
 917 therefore we can calculate the distance of a point from this segment analogically
 918 to Equation 4.25 with \mathbf{v} given as a unit vector in the direction of the segment.

919 We need to find the segment with the lowest distance. We assume, that
 920 the distance $d_{\mathbf{P}}(\tau)$ of a point \mathbf{P} to the point on the track $\mathbf{X}(\tau)$ has a single
 921 minimum (local and global), no local maximum (except the interval endpoints)
 922 and no saddle point

$$\exists! \tau_{\min} \in [0, \tau_N]: (\forall \tau \in [0, \tau_N]: d_{\mathbf{P}}(\tau) \geq d_{\mathbf{P}}(\tau_{\min})) \vee \frac{dd_{\mathbf{P}}}{d\tau}(\tau_{\min}) = 0, \quad (4.28)$$

923 where N is the number of RK4 steps. This is a reasonable assumption for a track
 924 with an approximate shape of a circular arc with a radius r , since the distance d
 925 from a point \mathbf{C} on the corresponding circle of a point \mathbf{P} offset by a from the arc
 926 plane and by b from the arc's center when projected on its plane is given by the
 927 law of cosines:

$$d^2 = a^2 + b^2 + r^2 - 2br \cos \alpha, \quad (4.29)$$

928 where α is the angle between points \mathbf{C} and \mathbf{P} as seen from the center of the arc
 929 (see Figure 4.5). This function is strictly convex for $\alpha \in (-\frac{\pi}{2}, \frac{\pi}{2})$ and in our case,
 930 the center of the arc lies outside of the detector and α is restricted to a small
 931 interval around zero (especially considering that the initial guess should make the
 932 fitted trajectory reasonably close to any relevant point, in the worst-case scenario,
 933 the distance is overestimated which should keep the fit from converging to such
 934 solutions).

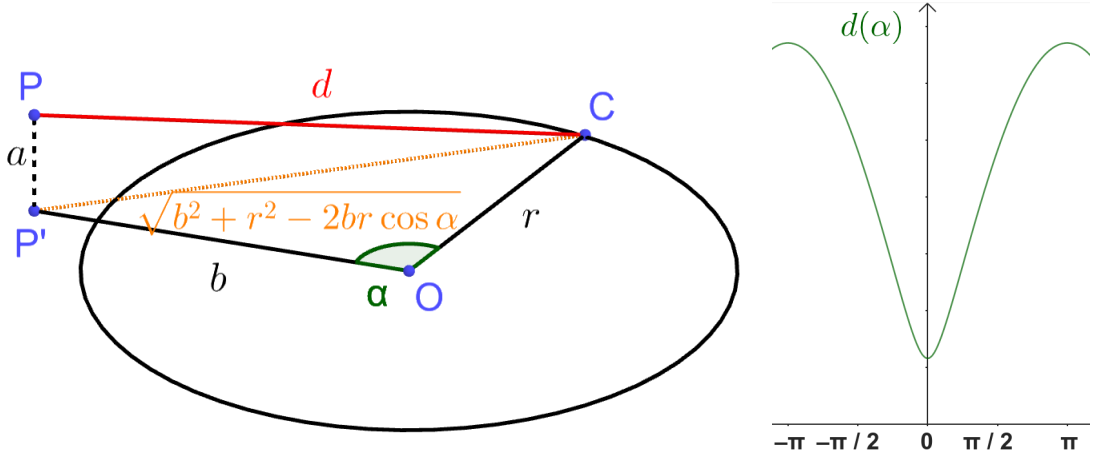


Figure 4.5: Demonstration of the convexity of the distance function $d(\alpha)$ for a circular track (see Equation 4.29).

935 In a more general case, if we consider the vector $\mathbf{a}(\tau) = \mathbf{P} - \mathbf{X}(\tau)$ whose size
936 is $\|\mathbf{a}(\tau)\| = d_{\mathbf{P}}(\tau)$, then we get

$$2d_{\mathbf{P}} \frac{dd_{\mathbf{P}}}{d\tau} = \frac{dd_{\mathbf{P}}^2}{d\tau} = \frac{d}{d\tau} \sum_i a_i^2 = 2 \sum_i a_i \frac{da_i}{d\tau} = 2\mathbf{a} \cdot \frac{d\mathbf{a}}{d\tau} = -2\mathbf{a} \cdot \frac{d\mathbf{X}}{d\tau}, \quad (4.30)$$

937 therefore for the derivative of $d_{\mathbf{P}}(\tau)$ to be zero, $\mathbf{a}(\tau)$ has to be perpendicular
938 to the tangent of the track. In 3D, for a given $\mathbf{X}(\tau)$, this condition restricts \mathbf{P}
939 to a plane. This means that for a curving track we can find a point \mathbf{P} for any
940 two points $\mathbf{X}(\tau), \mathbf{X}(\sigma)$ with non-parallel tangents that has $\frac{dd_{\mathbf{P}}}{d\tau}(\tau) = \frac{dd_{\mathbf{P}}}{d\tau}(\sigma) =$
941 $= 0$, which violates the assumption 4.28. If we have a circle-and-lines track as
942 described in the previous sections, such a point has to lie outside of the circular
943 sector given by the arc.

944 For a planar track, the envelope of all its normals is the evolute of the curve
945 (i.e., the set of centers of all its osculating circles). If the track has a monotonous
946 tangent angle

$$\alpha(\tau) = \text{atan} \frac{\frac{dX_2}{d\tau}}{\frac{dX_1}{d\tau}} \quad (4.31)$$

947 with minimal and maximal α differing by less than π (i.e., the track changes
948 direction by less than 180°), then all intersections of the track's normals must lie
949 on the side of the evolute closer to the track (not obvious?, sometimes the sides
950 are opposite?). At the same time, the intersection must lie in the half planes
951 given by the normals at the beginning and the end of the curve and pointing
952 away from the curve. Together, these three boundaries define a closed shape that
953 will lie outside of the OFTPC for a typical track in our detector.

954 With the assumption 4.28, we can find the segment on the RK4 track with
955 the lowest distance to a given point \mathbf{P} using a binary search algorithm. Let
956 the distance of the point from the n -th vertex be $d_{\mathbf{P},n}$. Then the difference
957 $\Delta d_{\mathbf{P},n} = d_{\mathbf{P},n} - d_{\mathbf{P},n-1}$ satisfies

$$\begin{aligned} \Delta d_{\mathbf{P},n} &< 0 \quad \forall n \text{ such that } \tau_n < \tau_{\min}, \\ \Delta d_{\mathbf{P},n} &> 0 \quad \forall n \text{ such that } \tau_{n-1} > \tau_{\min}. \end{aligned} \quad (4.32)$$

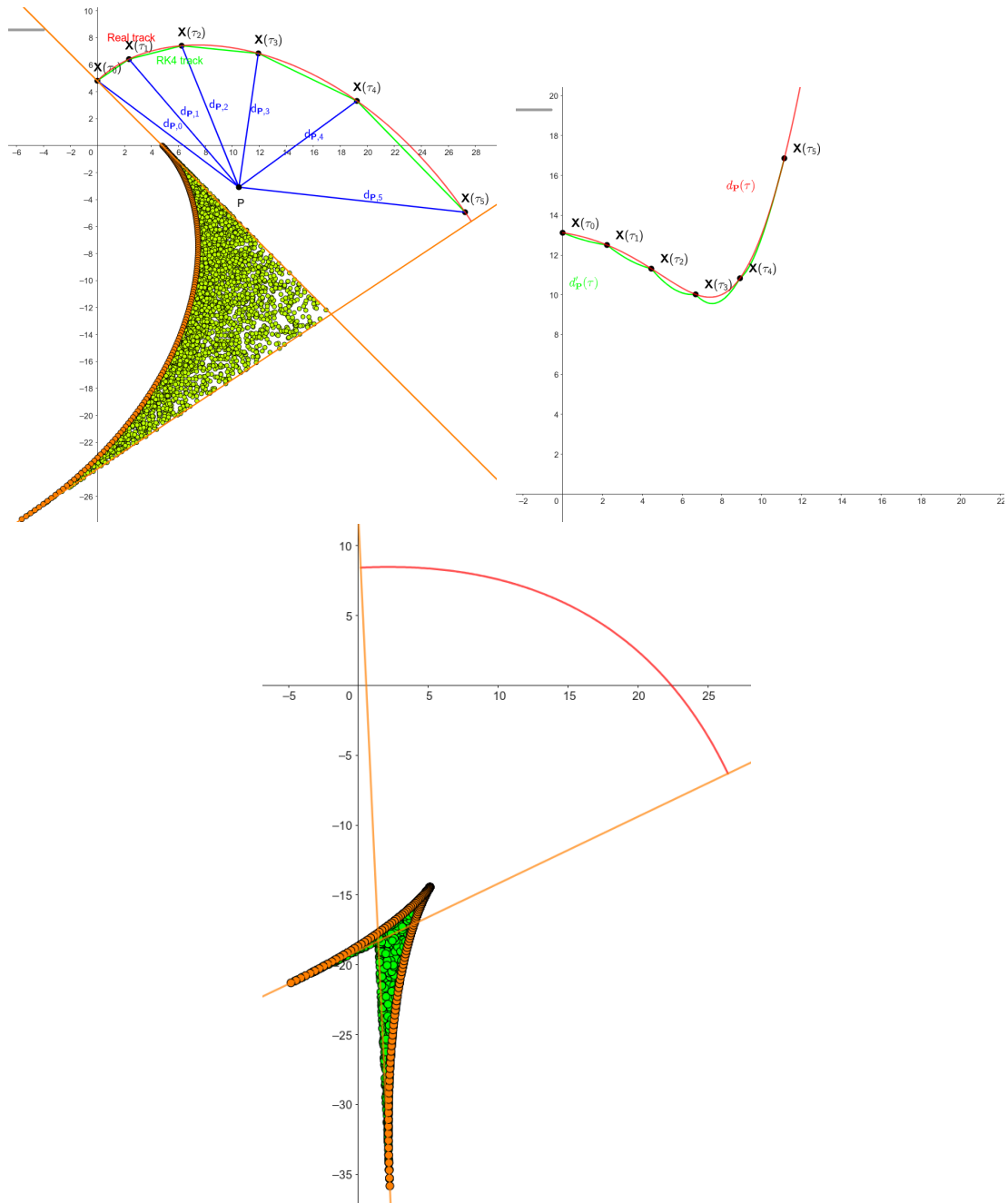


Figure 4.6: some provisional figures

Therefore, we can search for the segment containing $d_{\mathbf{P},\min}$ with binary search starting with $\Delta d_{\mathbf{P},1}$ and $\Delta d_{\mathbf{P},N}$, then calculate the difference $\Delta d_{\mathbf{P},m}$ for the middle index $m = \left\lfloor \frac{N+1}{2} \right\rfloor$. If $\Delta d_{\mathbf{P},m} > 0$ (minor bug in the implementation – if the value for the maximal index is negative, it shouldn't change anything), we can replace the higher index with m , otherwise we replace the lower index. The search stops when the difference between the minimal and maximal index is one. Would it be better if they were the same (maybe not)? Then the minimal value is $d_{\mathbf{P},n-1}$ or $d_{\mathbf{P},N}$ and we can take the minimum of the distances from the two segments connected to $n - 1$. Currently taking the maximal index (and starting at $N - 2$ maximal index $\leftrightarrow N - 1$ -th point), this should be equivalent, since either $\Delta d_{\mathbf{P},\max} > 0$ (in the code is equivalent to max-1 here) or we are at $N - 1$. The minimum of the two distances still taken.

Same details with MIGRAD etc. as previously.

Conclusion

972 Here or at the end of each section. Something about the future of this work?

973 Notes

974 General notes about the thesis:

- 975 • Check that all of the classes and other code are marked the same way in
976 the text. I used italics somewhere, could use different font for this instead.
- 977 • Check unbreakable space in front of articles. Remove excessive article usage
978 with proper nouns.
- 979 • Currently using margins for single-sided printing (bigger on the left side).
- 980 • Check that present tense is used
- 981 • Active vs passive voice usage
- 982 • American English quotation marks (") instead of British English (').
- 983 • Some of the overfull hbox warnings might change if duplex printing is used
984 (they generate black rectangles on the edge of the page), leaving them be
985 for now
- 986 • Check nobreakdash usage (is it always necessary)
- 987 • Check capitalized references (e.g., Figure, Section, Equation)
- 988 • Check \(...\mathbf{\backslash}\) math mode instead of \\$...\$. (actually unlike \[...\] math mode,
989 there is apparently no real benefit to this clumsy syntax)
- 990 • Use siunitx package to ensure correct formatting, physics package for deriva-
991 tives.
- 992 • Check other stuff that's written in the MFF UK template. Apparently it
993 has since been updated and there are some differences (check for them).
- 994 • Check correct subscripts in equation (italics vs no italics)
- 995 • Consistent bold marking of points/vectors
- 996 • Correct footnotes (capital letters, etc.).
- 997 • Might have to mention GeoGebra as per the non-commercial license agree-
998 ment (Made with GeoGebra®) – maybe put it into acknowledgments next
999 to the MetaCentrum credit? And list all of the figures where GeoGebra was
1000 used?
- 1001 • Maybe make some section outside of References specifically for literature?
1002 (such as the old CERN TPC review, ATOMKI review is currently not
1003 mentioned, not sure if some Wikipedia articles should get a mention or how
1004 do these things work)
- 1005 • Consistent use of `bm` vs `mathbf`

- Consistent use of $\bar{\mathcal{M}}$ instead of \mathcal{M} when talking about the map of the means (so most of the time)
 - Proper equation numbering when deriving a relation
 - Hugo should be mentioned somewhere in the title probably?
- Random notes:
- Terminology consistency – ionization/primary/secondary electrons
 - Consistent TPC vs OFTPC acronym usage in the text or individual chapters.
 - Only electrons that start and end in the sector closer than 0.5 cm are used for reconstruction (newest version).
 - Attachment, Penning transfer and secondary ionization not considered in the microscopic simulation.
 - Suspicious artifacts of trilinear interpolation in Figure 1.7. **Fixed – integers instead of doubles in the implementation, influenced reconstruction SIGNIFICANTLY (but not simulation).**
 - Profiling of the reconstruction!!!! Find out what's taking the most time (probably Runge-Kutta integration which the fit calls a lot). Could gradually decrease the step size to refine the fit instead of making it small right away (arbitrarily small – the effect of this was never tested). This could take some time to do properly (find a profiler or make profiling macros).
 - Slow drift velocity good for z reconstruction, too low leads to recombination
 - Could add link to the GitHub repository

Future

Things planned for the future:

- Testing the reconstruction algorithm by measuring real particles with a known energy distribution.
- The **Fast Simulation with Ionization Electron Map** is planned for the future. It will use the HEED program [29] to simulate the primary particle and the Ionization Electron Map (see Section 3.2) to simulate the drift of secondary electrons. It should be significantly faster than the Microscopic Simulation but offer comparable precision since it will rely on an already simulated drift map. (Primary track simulated in HEED. Readout parameters by interpolating the map. Diffusion from the map for randomization.)
- Account for GEM, delta electrons, ...
- Likelihood approach instead of least squares (if it improves the reconstruction significantly), we should at least use a better method than taking the center of the TPC bin.
- More detailed electric field simulation (if needed, GEM will have more complex field, some irregularities in the field should be considered)

- 1045 • Account for the triggering in MWPC/TPX3 (particle travels from TPX3
 1046 to MWPC basically immediately – fraction of a nanosecond so there should
 1047 be no significant difference)

1048 **Likelihood - inverse map**

1049 If we wanted to further improve this procedure, taking into account the whole
 1050 map \mathcal{M} , we could make an "inverse map" from \mathcal{R} to distributions on \mathcal{D} . We could
 1051 achieve this by taking the normalized probability density of an electron with initial
 1052 coordinates (x, y, z) having readout coordinates (x', y', t) . If we fix (x', y', t) , we
 1053 get an unnormalized probability density $f(x, y, z) = \mathcal{M}_{(x,y,z)}(x', y', t)$ (assuming
 1054 that all initial coordinates are a priori equally likely). This could potentially
 1055 improve the discrete reconstruction if we take the mean value of this probability
 1056 density across the pad and time bin

$$f_{\text{pad, bin}}(x, y, z) = \frac{1}{A_{\text{pad}} \Delta t_{\text{bin}}} \int_{\text{pad, bin}} \mathcal{M}_{(x,y,z)}(x', y', t) dx' dy' dt \quad (4.33)$$

1057 and using it for a likelihood fit instead of using least squares. This still assumes
 1058 that all initial coordinates are equally likely which is clearly not the case for
 1059 a primary particle track. In the future, we could even use the fast track simulation
 1060 with the map (should be possible to make around 1000 tracks per minute per core
 1061 with current settings), create a big set of tracks with reasonable parameters and
 1062 use these to get an approximation of the probability distribution of the detector
 1063 response. Some approximations would be necessary when interpreting the data to
 1064 decrease the degrees of freedom of this distribution (we would have to pick a set of
 1065 parameters and assume that some of them are independent). This could give us
 1066 an idea about the best achievable resolution (how significantly will the detector
 1067 response differ for a given change in energy). If the difference is significant, we
 1068 could try to further improve the likelihood fit.

Bibliography

1. *Garfield++* [<https://garfieldpp.web.cern.ch/garfieldpp/>]. [N.d.]. Accessed: 2023-05-18.
2. BRUN, Rene; RADEMAKERS, Fons. Root — An Object Oriented Data Analysis Framework. *Nucl. Instrum. Methods Phys. Res. Sect. A: Accel. Spectrom. Detect. Assoc. Equip.* 1997, vol. 389, no. 1–2, pp. 81–86. Available from DOI: 10.1016/s0168-9002(97)00048-x. Proceedings AIHENP'96 Workshop, Lausanne, Sep. 1996, See also <https://root.cern/>, Paper published in the Linux Journal, Issue 51, July 1998.
3. *About MetaCentrum* [<https://metavo.metacentrum.cz/en/about/index.html>]. 2023. Accessed: 2024-11-27.
4. ROSE, M. E. Internal Pair Formation. *Phys. Rev.* 1949, vol. 76, pp. 678–681. Available from DOI: 10.1103/PhysRev.76.678.
5. ESSIG, R. et al. *Dark Sectors and New, Light, Weakly-Coupled Particles*. 2013. Available from arXiv: 1311.0029 [hep-ph].
6. DE BOER, F.W.N. et al. A deviation in internal pair conversion. *Phys. Lett. B*. 1996, vol. 388, no. 2, pp. 235–240. ISSN 0370-2693. Available from DOI: [https://doi.org/10.1016/S0370-2693\(96\)01311-1](https://doi.org/10.1016/S0370-2693(96)01311-1).
7. BOER, F W N de et al. Excess in nuclear pairs near 9 MeV/ invariant mass. *J. Phys. G: Nucl. Part. Phys.* 1997, vol. 23, no. 11, p. L85. Available from DOI: 10.1088/0954-3899/23/11/001.
8. BOER, F W N de et al. Further search for a neutral boson with a mass around 9 MeV/c². *J. Phys. G: Nucl. Part. Phys.* 2001, vol. 27, no. 4, p. L29. Available from DOI: 10.1088/0954-3899/27/4/102.
9. VITÉZ, Attila et al. Anomalous Internal Pair Creation in ⁸Be as a Signature of the Decay of a New Particle. *Acta Phys. Pol. B - ACTA PHYS POL B*. 2008, vol. 39, p. 483.
10. KRASZNAHORKAY, A. et al. Searching for a light neutral axial-vector boson in isoscalar nuclear transitions. *Frascati Phys. Ser.* 2012, vol. 56, p. 86.
11. KRASZNAHORKAY, A. J. et al. Observation of Anomalous Internal Pair Creation in ⁸Be: A Possible Indication of a Light, Neutral Boson. *Phys. Rev. Lett.* 2016, vol. 116, no. 4. ISSN 1079-7114. Available from DOI: 10.1103/physrevlett.116.042501.
12. TILLEY, D.R. et al. Energy levels of light nuclei A=8,9,10. *Nucl. Phys. A*. 2004, vol. 745, no. 3, pp. 155–362. ISSN 0375-9474. Available from DOI: <https://doi.org/10.1016/j.nuclphysa.2004.09.059>.
13. SAS, N. J. et al. *Observation of the X17 anomaly in the ⁷Li(p,e⁺e⁻)⁸Be direct proton-capture reaction*. 2022. Available from arXiv: 2205.07744 [nucl-ex].
14. KRASZNAHORKAY, A. J. et al. New anomaly observed in ⁴He supports the existence of the hypothetical X17 particle. *Phys. Rev. C*. 2021, vol. 104, no. 4. ISSN 2469-9993. Available from DOI: 10.1103/physrevc.104.044003.

- 1111 15. TILLEY, D.R. et al. Energy levels of light nuclei A = 4. *Nucl. Phys. A*.
 1112 1992, vol. 541, no. 1, pp. 1–104. ISSN 0375-9474. Available from DOI: [https://doi.org/10.1016/0375-9474\(92\)90635-W](https://doi.org/10.1016/0375-9474(92)90635-W).
- 1114 16. KRASZNAHORKAY, A. J. et al. New anomaly observed in ^{12}C supports the
 1115 existence and the vector character of the hypothetical X17 boson. *Phys. Rev.*
 1116 *C*. 2022, vol. 106, p. L061601. Available from DOI: 10.1103/PhysRevC.106.
 1117 L061601.
- 1118 17. AJZENBERG-SELOVE, F. Energy levels of light nuclei A = 11,12. *Nucl. Phys.*
 1119 *A*. 1990, vol. 506, no. 1, pp. 1–158. ISSN 0375-9474. Available from DOI:
 1120 [https://doi.org/10.1016/0375-9474\(90\)90271-M](https://doi.org/10.1016/0375-9474(90)90271-M).
- 1121 18. KÁLMÁN, Péter; KESZTHELYI, Tamás. Anomalous internal pair creation.
 1122 *The Eur. Phys. J. A*. 2020, vol. 56. Available from DOI: 10.1140/epja/
 1123 s10050-020-00202-z.
- 1124 19. ALEKSEJEVS, A. et al. *A Standard Model Explanation for the "ATOMKI*
 1125 *Anomaly*". 2021. Available from arXiv: 2102.01127 [hep-ph].
- 1126 20. FENG, Jonathan L. et al. Protophobic Fifth-Force Interpretation of the Ob-
 1127 served Anomaly in ^8Be Nuclear Transitions. *Phys. Rev. Lett.* 2016, vol. 117,
 1128 p. 071803. Available from DOI: 10.1103/PhysRevLett.117.071803.
- 1129 21. ANH, Tran The et al. Checking the 8Be Anomaly with a Two-Arm Electron
 1130 Positron Pair Spectrometer. *Universe*. 2024, vol. 10, no. 4, p. 168. ISSN 2218-
 1131 1997. Available from DOI: 10.3390/universe10040168.
- 1132 22. ABRAAMYAN, Kh. U. et al. *Observation of structures at ~ 17 and ~ 38*
 1133 *MeV/c 2 in the $\gamma\gamma$ invariant mass spectra in pC, dC, and dCu collisions at*
 1134 *p_{lab} of a few GeV/c per nucleon*. 2023. Available from arXiv: 2311.18632
 1135 [hep-ex].
- 1136 23. COLLABORATION, The MEG II et al. *Search for the X17 particle in $^7\text{Li}(\text{p}, \text{e}^+\text{e}^-)^8\text{Be}$*
 1137 *processes with the MEG II detector*. 2024. Available from arXiv: 2411.07994
 1138 [nucl-ex].
- 1139 24. ABED ABUD, Adam et al. A Gaseous Argon-Based Near Detector to En-
 1140 hance the Physics Capabilities of DUNE. 2022. Available from DOI: 10.
 1141 48550/arXiv.2203.06281.
- 1142 25. LOKEN, Stewart C. et al. Performance of the Signal Processing System for
 1143 the Time Projection Chamber. *IEEE Trans. on Nucl. Sci.* 1983, vol. 30, no.
 1144 1, pp. 162–166. Available from DOI: 10.1109/TNS.1983.4332243.
- 1145 26. AHMED, Misbah Uddin. *Simulation of the electron and ion movement through*
 1146 *a 4-GEM stack*. 2021. Institut für Kernphysik.
- 1147 27. MARMELAD. *3D interpolation2.svg*. 2025. Available also from: https://commons.wikimedia.org/wiki/File:3D_interpolation2.svg. Licensed
 1148 under CC BY-SA 3.0 (<https://creativecommons.org/licenses/by-sa/3.0/legalcode>). Accessed: 9-April-2025.
- 1149 28. CMGLEE. *Trilinear interpolation visualisation*. 2025. Available also from:
 1150 https://commons.wikimedia.org/wiki/File:Trilinear_interpolation_visualisation.svg. Licensed under CC BY-SA 3.0 (<https://creativecommons.org/licenses/by-sa/3.0/legalcode>). Accessed: 26-March-2025.

1155 29. SMIRNOV, I.B. Modeling of ionization produced by fast charged particles in
1156 gases. *Nucl. Instrum. Methods Phys. Res. Sect. A: Accel. Spectrom. Detect.*
1157 *Assoc. Equip.* 2005, vol. 554, no. 1, pp. 474–493. ISSN 0168-9002. Available
1158 from DOI: <https://doi.org/10.1016/j.nima.2005.08.064>.

1159 **Acknowledgments:** Computational resources were provided by the e-INFRA
1160 CZ project (ID:90254), supported by the Ministry of Education, Youth and Sports
1161 of the Czech Republic.

List of Figures

1163	0.1	The ATOMKI anomalous IPC measured for different nuclei.	4
1164	0.2	Results from the Hanoi spectrometer – angular e^+e^- pair correlations measured in the ${}^7\text{Li}(p, e^+e^-){}^8\text{Be}$ reaction at $E_p = 1225$ keV [21].	5
1165	0.3	Results from the MEG II experiments – angular correlation of e^+e^- pairs with $E_{\text{sum}} \in [16, 20]$ MeV measured in the ${}^7\text{Li}(p, e^+e^-){}^8\text{Be}$ reaction with proton beam energies 500 and 1080 keV. The 500 keV dataset is fitted with Monte Carlo of both the IPC deexcitation and the EPC produced by gammas [23].	6
1166	0.4	Schematics of the detector at the Van der Graaff facility at IEAP CTU.	6
1172	1.1	Particle identification in the PEP-4 TPC at SLAC based on the energy loss per distance $\frac{dE}{dx}$ [24].	8
1173	1.2	Schematic view of the PEP-4 TPC [25]. A charged particle produced in a collision in the beam pipe creates a spiral ionization track in the magnetic field. The central cathode then accelerates ionization electrons towards the endcap anode wires where they are multiplied and read out.	9
1174	1.3	A scanning electron microscope image of a GEM foil. [Ref]	11
1175	1.4	Garfield simulation of an avalanche in a GEM hole [26]. An incoming electron (orange) is accelerated in the strong electric field of the GEM and causes further ionization multiplying the number of free electrons (orange). Most of the produced cations (red) are captured by the GEM cathode.	12
1176	1.5	Schematics of the first sector OFTPC with detector space coordinates.	14
1177	1.6	Pad layout of the OFTPC and its parameters. Pads 102, 124 and 127 are irregular, the rest has the same dimensions.	15
1178	1.7	Magnetic field simulation results. The OFTPC volume and the vacuum tube are marked with black lines, the magnets are marked with red lines. The coordinates of the magnets from the CAD drawing seem to be 9/10 of the ones from the magnetic simulation (confirm and fix).	16
1179	1.8	Visualization of trilinear interpolation as a composition of linear interpolations (inspired by [27]). We want to interpolate the value in the red point C. First we interpolate between the four pairs of blue points sharing the last two indices along the x -axis (Eq. 1.14), then between the two pairs of the resulting green points along the y -axis (Eq. 1.15) and finally between the two resulting orange points along the z -axis to get the final red value (Eq. 1.16).	17
1180	1.9	Geometric interpretation of trilinear interpolation as expressed in Equation 1.18. The colored dots represent the values in given points and the colored boxes represent the volume in the opposite corner by which the corresponding values are multiplied. The black dot represents the interpolated value which is multiplied by the entire volume [28].	17

1207	2.1 Example of a simulated electron track in 70 % argon and 30 % CO ₂ atmosphere (on the left). Swap for better images, better zoom. Explain drift lines, primary particle.	19
1208		
1209		
1210	2.2 Comparison of diffusion in a simulated electron track in 70 % argon, 30 % CO ₂ atmosphere and in 90 % argon, 10 % CO ₂ atmosphere (on the right). Swap for better image, better zoom. Or put the same pictures for both comparisons in one subfigure, etc. Describe better.	19
1211		
1212		
1213		
1214		
1215	3.1 Dependence of the drift time on the z coordinate in 90 % argon and 10 % CO ₂ atmosphere, fitted with a linear function. The fitted function gives us the average drift velocity in the gas and can be used for rough reconstruction in our TPC. Swap for better image with axis labels, etc. Maybe write the fitted equation.	23
1216		
1217		
1218		
1219		
1220	3.2 The first attempt of a track reconstruction using only the drift velocity. This approach works well in a standard TPC (ideally cite some source). 90 % argon and 10 % CO ₂ atmosphere. Swap for better image, correct coordinates.	24
1221		
1222		
1223		
1224	3.3 First attempt at a track reconstruction using only the drift velocity, residues. Swap for better image, correct coordinates. What's causing the shift? Explain details.	24
1225		
1226		
1227	3.4 Example of map generation. Swap for better image, correct coordinates.	27
1228		
1229	3.5 Example reconstruction with the map. Swap for better image, correct coordinates.	27
1230		
1231	3.6 Selection of the points for interpolation. Create better images; use the explanation interpolation vs. extrapolation strange property. Solution 2 probably does not make much sense.	30
1232		
1233		
1234	4.1 Example of a fitted reconstructed track. Swap for better image.	32
1235	4.2 First attempt at a track reconstruction using only the drift velocity. Spline energy reconstruction attempt. Swap for better image(s) – subfigure environment, correct coordinates.	34
1236		
1237		
1238	4.3 First attempt at a track reconstruction using only the drift velocity. Circle and Lines Fit in 2D. Swap for better image, correct coordinates. Bias should be described in the previous chapter, not here.	36
1239		
1240		
1241		
1242	4.4 Circle and Lines Fit 3D geometry. Swap for better image.	39
1243		
1244	4.5 Demonstration of the convexity of the distance function $d(\alpha)$ for a circular track (see Equation 4.29).	40
1245	4.6 some provisional figures	41

¹²⁴⁶ **List of Tables**

¹²⁴⁷ List of Abbreviations

- ¹²⁴⁸ **GEM** Gas Electron Multiplier
- ¹²⁴⁹ **HEED** High Energy Electro-Dynamics
- ¹²⁵⁰ **IEAP CTU** Institute of Experimental and Applied Physics, Czech Technical
¹²⁵¹ University in Prague
- ¹²⁵² **IPC** Internal Pair Creation
- ¹²⁵³ **EPC** External Pair Creation
- ¹²⁵⁴ **Micromegas** MICRO-MEsh GAseous Structure
- ¹²⁵⁵ **MWPC** Multi-Wire Proportional Chamber
- ¹²⁵⁶ **OFTPC** Orthogonal Fields TPC
- ¹²⁵⁷ **RK4** Runge-Kutta 4th order
- ¹²⁵⁸ **TPC** Time Projection Chamber
- ¹²⁵⁹ **ToA** time-of-arrival
- ¹²⁶⁰ **ToT** time-over-threshold
- ¹²⁶¹ **TPX3** Timepix 3